Earth Planets Space, **61**, 411–430, 2009

The spread *F* Experiment (SpreadFEx): Program overview and first results

D. C. Fritts[1], M. A. Abdu[2], B. R. Batista[2], I. S. Batista[2], P. P. Batista[2], R. Buriti[3], B. R. Clemesha[2], T. Dautermann[4], E. de Paula[2], B. J. Fechine[2], B. Fejer[5], D. Gobbi[2], J. Haase[4], F. Kamalabadi[6], B. Laughman[1], L. M. Lima[7], H.-L. Liu[8], A. Medeiros[3], P.-D. Pautet[2,5], D. M. Riggin[1], F. São Sabbas[2], J. H. A. Sobral[2], P. Stamus[1], H. Takahashi[2], M. J. Taylor[5], S. L. Vadas[1], and C. M. Wrasse[9]

[1]*NorthWest Research Associates, Colorado Research Associates Division, Boulder, CO*
[2]*Instituto Nacional de Pesquisas Espaciais (INPE), São José dos Campos, Brazil*
[3]*Universidade Federal de Campina Grande, Campina Grande, Paraíba, Brazil*
[4]*Purdue University, West Lafayette, IN*
[5]*Utah State University, Logan, UT*
[6]*University of Illinois, Urbana, IL*
[7]*Universidade Estadual da Paraíba, Campina Grande-PB, Brazil*
[8]*National Center for Atmospheric Research, Boulder, CO*
[9]*IP&D—Universidade do Vale do Paraíba—UNIVAP, São José dos Campos—SP, Brazil*

(Received July 27, 2007; Revised February 13, 2008; Accepted June 3, 2008; Online published May 14, 2009)

We performed an extensive experimental campaign (the spread *F* Experiment, or SpreadFEx) from September to November 2005 to attempt to define the role of neutral atmosphere dynamics, specifically wave motions propagating upward from the lower atmosphere, in seeding equatorial spread *F* and plasma bubbles extending to higher altitudes. Campaign measurements focused on the Brazilian sector and included ground-based optical, radar, digisonde, and GPS measurements at a number of fixed and temporary sites. Related data on convection and plasma bubble structures were also collected by GOES 12 and the GUVI instrument aboard the TIMED satellite. Initial results of our analyses of SpreadFEx and related data indicate 1) extensive gravity wave (GW) activity apparently linked to deep convection predominantly to the west of our measurement sites, 2) the presence of small-scale GW activity confined to lower altitudes, 3) larger-scale GW activity apparently penetrating to much higher altitudes suggested by electron density and TEC fluctuations in the *E* and *F* regions, 4) substantial GW amplitudes implied by digisonde electron densities, and 5) apparent direct links of these perturbations in the lower *F* region to spread *F* and plasma bubbles extending to much higher altitudes. Related efforts with correlative data are defining 6) the occurrence and locations of deep convection, 7) the spatial and temporal evolutions of plasma bubbles, the 8) 2D (height-resolved) structures of plasma bubbles, and 9) the expected propagation of GWs and tides from the lower atmosphere into the thermosphere and ionosphere.
Key words: Equatorial spread *F*, plasma instabilities, plasma bubbles, plasma bubble seeding, thermospheric gravity waves.

1. Introduction

Considerable progress has been made in recent years in understanding the occurrence, morphology, and variability of equatorial spread *F* (ESF) and plasma bubbles penetrating to higher altitudes. Despite this, an understanding of the conditions seeding ESF and plasma bubbles has remained elusive, with neither observations nor theory sufficiently comprehensive or persuasive to be definitive. Computed Rayleigh-Taylor Instability (RTI) growth rates based on known flow structures are typically too small, and it is unclear whether seeding can be entirely a plasma process or whether neutral perturbations are necessary to enhance plasma instability growth rates. Gravity waves (GWs) have been suggested as a trigger in many studies, either directly via density and/or velocity perturbations at the bottomside *F* layer or indirectly via mapping of electric field or other field-line-integrated perturbations generated by GWs interacting with sporadic *E* (E_s) layers or other fields at lower altitudes off the dip (magnetic) equator. However, definitive proof of GW seeding, the "smoking gun", observational or theoretical, has yet to be found. These issues motivated a combined experimental, modeling, and theoretical program initiated with two field campaigns performed in Brazil during "moon down" conditions from September to November 2005. Our measurements employed a suite of airglow cameras, VHF and meteor radars, digisondes, and GPS receivers at a number of fixed and temporary sites and correlative measurements with the Jicamarca Radio Observatory in Peru and via satellite (GUVI aboard TIMED and CHAMP) to characterize the neutral atmosphere and ionosphere as fully as possible during these periods. The primary goal of the spread *F* Experiment (SpreadFEx) was to test the theory that GWs play an essential role in the seeding of ESF and plasma bubbles extending to much higher altitudes. The purpose of this paper is to summarize our experimental design and describe our initial analysis results.

More detailed analyses of SpreadFEx data, supporting theoretical studies, and assessments of specific potential GW influences at bottomside *F* layer altitudes will appear in a forthcoming SpreadFEx special issue of *Annales Geophysicae*.

We begin in Section 2 by reviewing what is known of ESF and plasma bubble dynamics based on ∼30 years of observations, modeling, and theory, and what we understand of GW excitation and propagation into the thermosphere/ionosphere (TI). Our SpreadFEx campaign objectives and measurement strategy employed for our two field campaigns and an overview of our initial analyses are described in Sections 3 and 4. Section 5 provides a discussion of potential direct GW contributions to ESF and plasma bubble seeding at the bottomside *F* layer, as these are the only contributions we can assess within the scope of this overview. A summary of our initial results is presented in Section 6. The majority of the data discussed here are from 24 to 27 October 2005 during our second SpreadFEx campaign interval. However, some of these data (particularly airglow and some GPS measurements) were collected under clear skies during our first campaign interval.

2. Summary of Previous Studies

2.1 ESF and plasma bubbles

ESF on the bottomside of the *F* layer yields ionosonde signatures virtually every night of its occurrence season. Strong ESF and plasma bubbles typically arise during the pre-reversal enhancement (PRE) of the zonal electric field when upward $\mathbf{E} \times \mathbf{B}$ plasma drifts elevate the *F* layer sufficiently (Heelis *et al*., 1974; Fejer *et al*., 1999). RTI is believed to be responsible for these plasma instabilities, and nonlinear RTI growth causes flux tube-aligned plasma depletions to rise to the topside ionosphere, where they may attain equatorial apex heights of ∼1000–1500 km in well developed cases. Plasma bubbles that penetrate to high altitudes occur on only ∼30 to 60% of nights, are apparently uncorrelated at closely spaced longitudes, but may share seeding conditions, and exhibit seasonal, solar-cycle, geographic, and geomagnetic dependencies (McClure *et al*., 1977; Sobral *et al*., 1980a, b, 2002; Mendillo and Tyler, 1983; Abdu *et al*., 1992; Aggson *et al*., 1992; McClure *et al*., 1998; Fejer *et al*., 1999; Sobral *et al*., 2001; Hysell and Burcham, 2002; Rodrigues *et al*., 2004; Stolle *et al*., 2006; Su *et al*., 2008). In particular, increasing solar flux correlates with greater PREs of plasma drift, earlier ESF seeding and irregularity appearance, and higher initial altitudes (Hysell and Burcham, 2002).

GWs are potentially important in providing modulations of plasma densities, velocities, and electric fields needed to seed RTI via either 1) direct neutral density and horizontal and/or vertical velocity perturbations at the bottomside *F* layer or 2) GW-plasma interactions at lower altitudes that create plasma density, velocity, and/or electric field perturbations that map to higher altitudes (Woodman and LaHoz, 1976; Kelley *et al*., 1981; Anderson *et al*., 1982; Valladares *et al*., 1983; Kelley, 1989; Hysell *et al*., 1990; Kelley and Hysell, 1991; Huang *et al*., 1993; Huang and Kelley, 1996a, b, c; Sekar and Kelley, 1998; Taylor *et al*., 1998; Prakash, 1999; Tsunoda, 2005, 2006, 2007). GW perturbations have been suggested to lead to local current and electric field fluctuations having the wavelength of the GW (Klostermeyer, 1978; Kelley, 1989). More recently, GW interactions with sporadic *E* (E_s) layers were suggested by Prakash (1999) to yield electric field perturbations that map efficiently to the bottomside *F* layer; a related mechanism involves the mapping of large-scale polarization electric fields arising from E_s layer instability to these same altitudes (Tsunoda, 2005, 2006, 2007). These fluctuations are suggested to seed RTI extending to greater altitudes. Major challenges to these proposed mechanisms, however, are apparent random associations of E_s layers and ESF (Batista *et al*., 2008).

Observed plasma bubble scales and modeled initial conditions vary considerably, but are typically in the range of 10's to 100's of km in the plane normal to the magnetic field (Ossakow, 1981; Tsunoda, 1981; Haerendel *et al*., 1992; Sultan, 1996), seeding altitudes are ∼200 to 300 km at the dip equator, but may be 100 km or more lower away from the dip equator, and perturbations must apparently be sufficiently aligned along magnetic field lines so as to yield a field-line-integrated perturbation of sufficient magnitude (Huang and Kelley, 1996c). Indeed, GW density perturbations of a few % or vertical velocity perturbations of a few m s^{-1} are critical seed elements in models that have sought to describe RTI and plasma bubble growth and morphology to date (Huang and Kelley, 1996a, b). We also note that the anticipated arrival time at the bottomside of the *F* layer of large-amplitude GWs arising from tropical convection is ∼1 to 2 hours after maximum convective activity (Vadas and Fritts, 2004) and coincides closely with early evening times of strong ESF and bubble onset (Swartz and Woodman, 1998).

Because of the field-aligned nature of plasma fluctuations, much of the modeling of ESF and plasma bubbles has been two-dimensional (2D). These efforts captured some of the gross features of the morphology and examined sensitivity to seeding conditions and scales (Scannapieco and Ossakow, 1976; Keskinen *et al*., 1980; Zalesak and Ossakow, 1980; Hysell *et al*., 1990; Huang *et al*., 1993; Sekar *et al*., 1995). Other efforts accounted approximately for variations of key parameters along the magnetic field (and with altitude) and for key observed ESF and bubble features via field-line-integrated methods (Zalesak *et al*., 1982; Keskinen *et al*., 1998). Fully three-dimensional (3D) linear and nonlinear studies have been performed more recently that have delineated the impacts on growth rates and structure and yielded reasonable agreement with observations (Basu, 2002; Keskinen *et al*., 2003). The study by Keskinen *et al*. (2003) also reproduced bubble structures with sharp density gradients extending up to the equatorial anomaly.

Studies specific to GW seeding of strong ESF and plasma bubbles have examined the necessary conditions for such seeding and the structure of resulting plasma bubbles, including dependence on GW amplitudes and zonal wavelengths, the implications of initial amplitudes for RTI enhancements, the need (or lack of) for spatial resonance, the influences of zonal shear on plasma bubble scales and depths, and the impact of Pedersen conductivity on GW-induced perturbations (Hysell *et al*., 1990; Huang *et al*.,

1993; Sekar *et al.*, 1995; Huang and Kelley, 1996a, b, c; Sekar and Kelley, 1998). These studies have addressed the physical mechanisms enabling GW seeding of ESF and plasma bubbles. Another statistical study of potential GW seeding by McClure *et al.* (1998) demonstrated potentially significant correlations between regions of enhanced (depleted) *F* region irregularity occurrence and regions of anticipated strong (weak) tropical convection. They even noted that an anomalous enhancement accompanied enhanced convection and sea surface temperatures during a major El Nino. Thus, statistical correlations suggest the potential importance of the mechanisms modeled by various groups and point to deep tropical convection as a potentially important source of such GW perturbations.

2.2 ESF and RTI growth rates

Numerous theoretical efforts have addressed the neutral and plasma conditions contributing to ESF and RTI growth rates. While various theories have provided insights into the likely environments favoring ESF, RTI, and plasma bubble formation, they have also frequently failed to yield sufficiently large growth rates for plausible large-scale neutral and plasma flows. This has been a large part of the motivation for invoking GW perturbations, as one component of the geophysical noise spectrum, in the seeding of RTI and plasma bubbles. Most previous efforts have addressed RTI growth rates, which depend largely on the plasma environment, but with potential GW influences exerted either directly at the bottomside *F* layer or at lower altitudes that then map to the bottomside *F* layer (Ossakow, 1981; Zalesak *et al.*, 1982; Sultan, 1996; Prakash, 1999; Abdu, 2001; Tsunoda, 2005, 2006, 2007). However, a recent series of studies has considered an alternative instability mechanism depending directly on the neutral zonal wind that appears to achieve sufficiently large growth rates that explicit GW seeding of instabilities was suggested not to be required (Kudeki and Bhattacharyya, 1999; Hysell and Kudeki, 2004; Hysell *et al.*, 2004, 2005; Kudeki *et al.*, 2007).

A flux tube-integrated version of the generalized RTI linear growth rate based on Sultan (1996) can be written as

$$\gamma_{\rm FT} = \frac{\Sigma_{\rm P}^{F}}{\Sigma_{\rm P}^{E} + \Sigma_{\rm P}^{F}} \left(\frac{E}{B} - U_{\rm FT}^{\rm P} + \frac{g}{\nu_{\rm eff}} \right) \frac{1}{L_{\rm FT}} - \beta_{\rm FT} \qquad (1)$$

where E is the zonal electric field (which arises from the evening PRE in the zonal electric field due to *F* layer dynamo), g is the acceleration due to gravity, $\Sigma_{\rm P}^{E,F}$ are the field line integrated conductivities for the *E*- and *F*-region segments of a field line, $U_{\rm FT}^{\rm P}$ is the conductivity-weighted, flux tube-integrated vertical wind (normal to B), $L_{\rm FT}$ is the length scale of the density gradient, β is the recombination loss rate, $\nu_{\rm eff}$ is the effective ion-neutral collision frequency, and subscripts FT stand for flux tube-integrated quantities. In Eq. (1), GW influences can only be expressed through their impacts on the various plasma quantities affecting the RTI growth rate.

An alternative theory for preconditioning the bottomside *F* layer for ESF initiation and RTI claimed by the authors to *not* require GW seeding (Kudeki *et al.*, 2007) yields a growth rate

$$\gamma \sim \frac{U_{\rm n} - U_{\rm p}}{2L} \qquad (2)$$

where $U_{\rm n}$ and $U_{\rm p}$ are the zonal (eastward) neutral and plasma velocities and L is the length scale of the density gradient. These conditions differ in important respects from those considered previously to be key to RTI growth itself. The dominant requirements appear to be 1) a significant eastward neutral wind at the bottomside *F* layer, 2) a westward plasma drift at these altitudes, such that the eastward wind in the plasma coordinate is $U \sim 200$ m s^{-1}, and 3) a vertical plasma gradient having an effective scale length of $L \sim 20$ km or less. Kudeki *et al.* (2007) have argued that such conditions favor an instability having a westward phase tilt with altitude of 45° induced via vertical Pederson currents. The obvious question, to be addressed further in Section 5, is whether GWs can contribute meaningfully to, or modulate, this latter mechanism, either through initial conditions or altered growth rates or both. We focus on the latter mechanism here because we can easily estimate direct GW influences at the bottomside *F* layer, but are unable to easily assess the potentially competitive mechanisms involving the creation of electric fields at $E_{\rm s}$ layers at lower altitudes and their mapping to the bottomside *F* layer in this initial SpreadFEx overview. More detailed assessments of GW influences on plasma dynamics and instabilities will be provided in our SpreadFEx special issue (see, in particular, Fritts *et al.*, 2008a, b; Abdu *et al.*, 2008; Kherani *et al.*, 2008).

2.3 GWs in the thermosphere/ionosphere

GWs are now understood to play a number of key roles in neutral atmosphere dynamics extending from the Earth's surface into the lower thermosphere (LT). GW effects in the mesosphere and lower thermosphere (MLT) are well documented and arise due to the attainment of large amplitudes, transports of energy and momentum from sources at lower altitudes, and turbulence, mixing, and flux divergences accompanying instability processes. The roles of GWs in ionospheric and plasma processes, in contrast, are less well known but also potentially important. As in the neutral atmosphere, GW importance in the ionosphere hinges on their penetration to high altitudes and their attainment of large amplitudes. GWs have been suggested to play a role in the seeding of RTI, strong ESF, and plasma bubbles penetrating to high altitudes, though their roles continue to be debated and definitive observational evidence has yet to emerge.

Of the various sources of GWs in the MLT, deep tropical convection is arguably one of the most significant, correlating with enhanced variances in the stratosphere (Tsuda *et al.*, 2000) and with GWs having large amplitudes and penetrating to and well above the mesopause (Taylor and Hapgood, 1988; Piani *et al.*, 2000; Lane *et al.*, 2001; Sentman *et al.*, 2003; Vadas and Fritts, 2004, 2005, 2006; Vadas, 2007). Models of GW structure at OH airglow altitudes (~87 km) that arise from convection are able to describe the qualitative character and some of the more quantitative aspects of the observed GW field quite well. Importantly, tropical sources apparently remain competitive with the auroral zones even at very high altitudes (Hocke and Schlegel, 1996). Convection does not obviously explain all

of the GWs apparently propagating to high altitudes in the TI, however. Evidence of such motions in ISR data from Arecibo Observatory and the MU radar suggest penetration to much higher altitudes than implied for the spatial scales typically arising from convection (Oliver *et al*., 1997; Djuth *et al*., 1997, 2004). This, and the inability to excite and propagate GWs having very large spatial scales from the lower atmosphere, suggest an additional source in the MLT, likely secondary GW generation due to GW instability and mean-flow interactions (Vadas and Fritts, 2001, 2002; Vadas *et al*., 2003; Vadas, 2007; Fritts and Vadas, 2008).

GWs arising from individual convective plumes having frequencies of $\omega \sim N/3$, where N is the buoyancy frequency, can penetrate to lower thermospheric altitudes of ∼150 to 200 km altitudes under solar minimum conditions (Vadas and Fritts, 2004, 2005, 2006). Under solar maximum conditions, during which thermospheric densities increase and kinematic viscosities decrease dramatically, the same sources yields GWs that can penetrate to substantially higher altitudes (Vadas and Fritts, 2006; Vadas, 2007). Larger-scale GWs, likely *not* arising from individual convective plumes but rather as secondary radiation at higher altitudes, can penetrate to substantially higher altitudes under all solar conditions (Vadas, 2007). Together, these GW sources yield perturbations that span the spatial scales observed in plasma bubbles, horizontal scales of ∼40 to 400 km, and may reach substantial amplitudes at higher altitudes (Fritts and Vadas, 2008). Despite their small amplitudes at lower altitudes, the ∼5 to 15 scale heights between GW source regions and the bottomside F layer, and an expected suppression of GW instability processes that constrain amplitudes at lower altitudes (by the exponentially increasing kinematic viscosity), appear to allow GW perturbations to be large at the bottomside F layer. Specifically, horizontal and vertical winds, vertical displacements, and perturbation electron densities and electric fields due to GWs will likely be substantial at these altitudes (see below). While our SpreadFEx results to date are preliminary, it appears difficult at this stage to argue that GW perturbations cannot make plausible contributions to ESF and plasma bubble seeding conditions. Indeed, we believe that our initial data analyses, summarized below, suggest a significant role for neutral atmospheric waves in general and GWs in particular. These results will be elaborated further by Abdu *et al*. (2008), Fritts *et al*. (2008b), and Kherani *et al*. (2008) in the SpreadFEx special issue of *Annales Geophysicae*.

3. Overview of the Spread *F* Experiment (SpreadFEx)

The primary goal of SpreadFEx was to perform observational and modeling studies that would quantify the potential roles of GWs in seeding ESF and RTI in the bottomside F layer leading to plasma bubbles penetrating to higher altitudes. Because of the statistical links of plasma bubbles to tropical convection, we designed an experiment that would provide sensitivity to both neutral atmosphere responses to deep convection and plasma instabilities and structures at higher altitudes over Brazil. The specific link envisioned

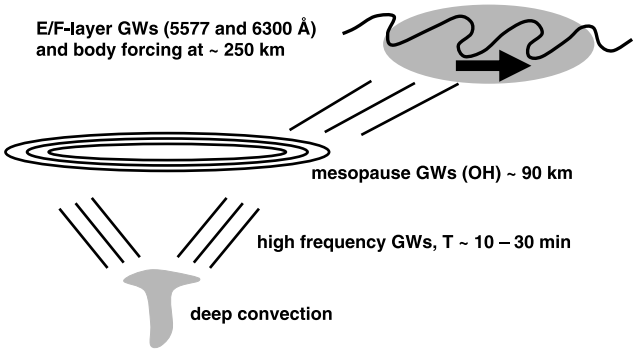

Fig. 1. Cartoon of GWs arising from deep convection, their penetration into the TI, and their potential contributions to ESF, RTI, and plasma bubble seeding.

was via GW coupling from deep convection, with both GW perturbations and mean responses contributing to potential seeding of ESF, RTI, and plasma bubbles at higher altitudes, as depicted in Fig. 1. Specific questions motivating these efforts include

1) Do GWs play a significant role in the generation of ESF and plasma bubbles at greater altitudes?
2) How do GW perturbations to the bottomside F layer alter the seeding conditions conducive to RTI and ESF generation?
3) If GWs are an important component of ESF and bubble generation, what are the geophysical parameters controlling their influences?
4) Are the GW roles in ESF and bubble generation sufficiently correlated with other measured geophysical parameters to allow a parameterization of these roles?

To address these issues, we designed a research program comprising three components. The first component was experimental, and included two measurement campaigns during "moon down" conditions from 25 September to 10 October and from 23 October to 8 November 2005. These measurement campaigns employed a suite of airglow cameras, VHF and meteor radars, digisondes, and GPS receivers at a number of fixed and temporary sites, as well as correlative measurements via satellite (GOES 12 and GUVI aboard TIMED) to characterize the neutral atmosphere and ionosphere as fully as possible during these periods. The second component of SpreadFEx was a series of analysis efforts. A third component included modeling of GW excitation and propagation in response to deep convection and plasma simulations of GW seeding to aid in the interpretation of our field data.

Our field measurements were performed in central and eastern Brazil and employed ground-based optical and radar instrumentation in collaboration with colleagues at Instituto Nacional de Pesquisas Espaciais (INPE) in Brazil, Utah State University (USU), and Purdue University (PU). INPE optical and radar instrumentation was located at several fixed sites, including São Luis, Fortaleza, Cariri, and Cachoeira Paulista extending from ∼2 to 23°S geographic latitude and from ∼0 to 17°S magnetic latitude, with GPS instrumentation more widely distributed. Additional tempo-

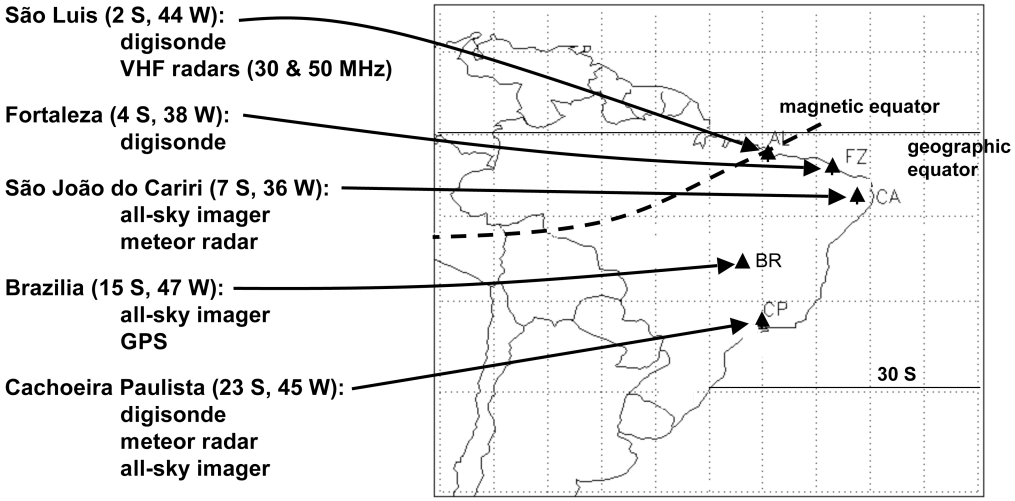

Fig. 2. Measurement sites in Brazil employed for the SpreadFEx measurement campaigns. GPS receivers were much more widely distributed, with ∼25 sites available for SpreadFEx.

Table 1. Instrumentation at the fixed INPE and temporary SpreadFEx measurements sites employed for our experiment. GPS were also available at ∼20 other locations in Brazil.

Site	Geogr. latitude	Magnetic latitude	Airglow	VHF radars	Meteor radars	Digisonde	GPS
São Luis	2.6 S	1.5 S		X		X	X
Fortaleza	3.9 S	5 S				X	X
Cariri	7.4 S	8 S	X		X		X
Fazenda Isabel	15 S	9 S	X				X
Cach. Paulista	22.7 S	17 S	X		X	X	X

rary optical and GPS measurements were made at Fazenda Isabel north of Brasilia and several nearby sites. Specifically, VHF radars at São Luis defined ESF altitudes and plasma bubble structures at the magnetic equator (de Paula and Hysell, 2004), meteor radars defined MLT winds at Cariri and Cachoeira Paulista (Batista *et al*., 2004; Buriti *et al*., 2007), digisondes defined electron densities at several dip latitudes (Batista and Abdu, 2004), airglow cameras defined both GW structures at MLT altitudes and plasma bubble structures at higher altitudes in the thermosphere at several locations south of the magnetic equator in order to assess the spatial and temporal variability of these processes (Medeiros *et al*., 2004), and GPS sensors were employed to attempt to define the spatial and temporal variations in electron densities (Lanyi and Roth, 1988). The instrument locations and their relation to the magnetic equator are shown in Fig. 2 and listed in Table 1.

4. Initial Results from SpreadFEx

4.1 Convection, GW sources and propagation

4.1.1 GOES 12 indications of deep convection GOES 12 visible, IR, and water vapor measurements over Brazil (at 1-, 4-, and 8-km resolutions, respectively) provided the best way to quantify the locations, scales, and intensities of deep convection leading to GW generation and propagation to higher altitudes during SpreadFEx. Cold cloud-top temperatures indicate deep convection, and temporal variations between successive images provide an indication of updraft intensities and durations. These data are being employed to estimate the spatial and temporal scales of convective plumes that are assumed to launch GWs propagating into the MLT and to higher altitudes. An example of the GOES 12 IR data showing deep convection, color-coded to highlight the coldest convective plumes, is shown for reference in Fig. 3. This image shows a number of regions of active, deep convection. Five exhibit extensive cold temperatures, assumed to be the largest and most mature convection, and the major sources of GWs at this time. These occur near (2°S, 68.5°W), (2.5°S, 67°W), (6°S, 62°W), (8.5°S, 62°W), and (10°S, 50.5°W). Brasilia is at (15°S, 47°W), our temporary optical site was ∼100 km north, and the dip equator is shown for reference. There are also a series of smaller cells having cold cloud tops, but smaller spatial scales, a number of which would also be actively exciting additional GWs. The largest and deepest convection is the most efficient source of GWs that penetrate to the highest altitudes, but the horizontal extent of the cloud top IR signatures often overestimates convective plume widths due to their generation of cirrus cloud shields as they mature. Indeed, recent high-resolution numerical studies by Lane *et al*. (2003) and Lane and Sharman (2006) show that such large-scale convection is often modulated by smaller-scale ∼5-km plumes.

4.1.2 Ray tracing of GWs into the TI Based on initial assessments of plume scales in the GOES 12 imagery, the five dominant convective plumes seen in Fig. 3 were assumed to have full-width, half maximum (FWHM) spatial scales of (10, 10, 5) km for the 1st, 2nd, and 4th plumes,

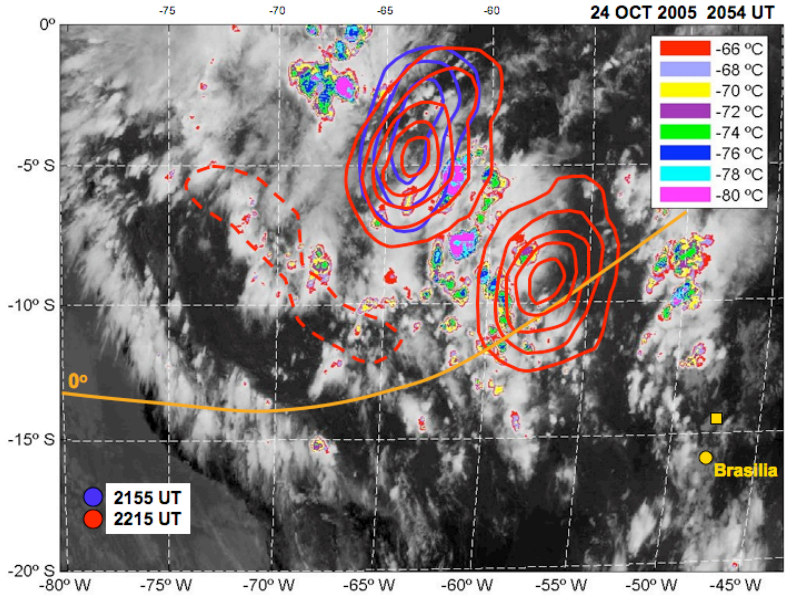

Fig. 3. GOES 12 convection observed in the IR channel at 20:54 UT on 24 October 2005. Cloud top temperatures are color coded, with solid (dashed) contours showing eastward (westward) GW momentum fluxes predicted at 21:55 (blue) and 22:15 (red) UT at 200 km. The dominant GW propagation at 200 km was eastward at this altitude due to filtering of GWs by strong westward winds at lower altitudes. Our temporary optical site for SpreadFEx was ∼100 km north of Brasilia (shown with the yellow square).

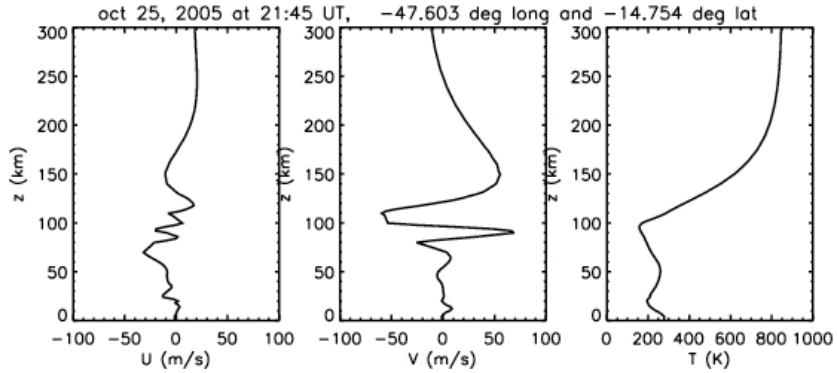

Fig. 4. Zonal (left) and meridional (center) wind and temperature (right) profiles at (47.6°W, 14.75°S) and 21:45 UT used for ray tracing GWs arising from the deep convective plumes observed in Fig. 3. The profiles were defined by balloon soundings below 30 km, meteor radar observations between 80 and 100 km, and a TIME GCM simulation initialized with the NCEP reanalysis data for this same period from 35 to 70 km and from 110 to 350 km, with linear interpolation elsewhere.

and (5, 5, 5) km for the 3rd and 5th plumes listed above. Assumed updraft velocities for the five were 30, 30, 35, 30, and 15 m s^{-1}, respectively. GWs assumed to arise from these plumes were ray traced from an assumed source altitude of 14 km upward through the zonal and meridional wind fields and a temperature field defined in the following manner. Balloon data were used to specify these fields from the surface to 30 km, meteor radar data from Cariri were used to define the low-frequency wind field between 80 and 110 km, and data from a thermosphere-ionosphere-mesosphere-electrodynamics (TIME) general circulation model (GCM) simulation, initialized with National Center for Environmental Prediction (NCEP) reanalysis data for this interval, were used to define the large-scale wind and temperature fields between 35 and 80 km, and again between 110 and 350 km. The resulting wind and temperature profiles used for this purpose are shown at (45°W, 10°S) in Fig. 4. There is, however, considerable variability in the wind field, and the GWs that survive to the highest altitudes are thus very sensitive to their source scales and locations. The resulting GWs were ray traced using the methodology of Vadas and Fritts (2004) and incorporated viscous dissipation at higher altitudes to assess maximum penetration altitudes (Vadas and Fritts, 2005).

Of the spectrum of GWs arising from each of the dominant convective sources, only a small fraction having suitable propagation directions and relatively large horizontal scales succeeded in surviving to 200 km altitude. The momentum flux distributions accompanying the surviving GWs for all five sources are contoured in Fig. 3 at 21:55 and 22:15 UT, the first time approximately an hour after GW generation. Note that the earlier responses (blue contours) are due to GWs having smaller horizontal wavelengths (∼100±50 km) and higher frequencies, hence higher vertical group velocities, with the response at later times (red contours) having slightly larger horizontal wave-

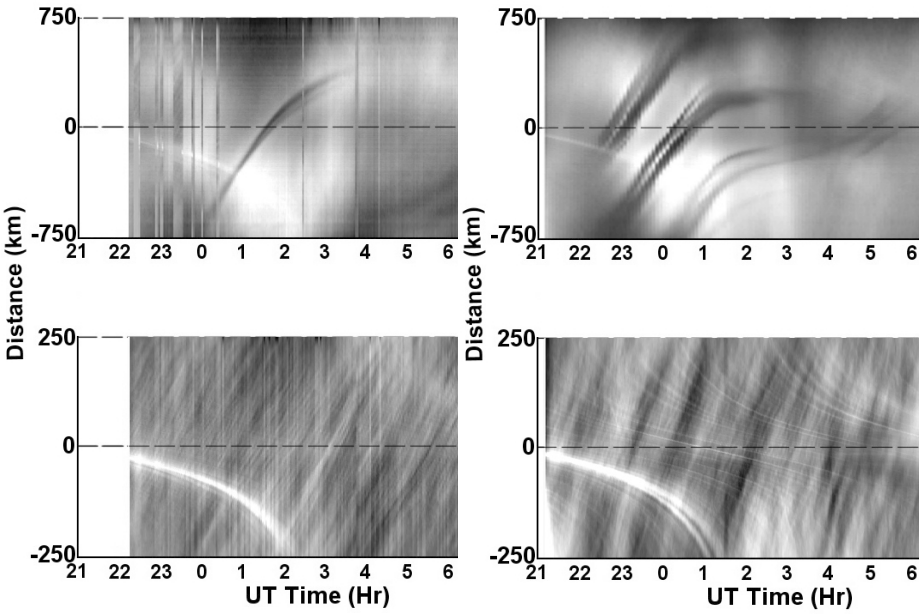

Fig. 5. Keograms prepared from east-west slices of 6300 Å (top) and OH (bottom) airglow emissions obtained at Brasilia (left) and Cariri (right) on 1 October 2005. Note that movement of structures in both emissions is generally eastward, but is faster and at ∼100 to 500-km zonal wavelengths in the TI and slower and at ∼20 to 400-km zonal wavelengths in the MLT

lengths (∼115±70 km) and occurring at larger distances from the convective sources. The earlier response is composed largely of westward-propagating GWs having negative zonal momentum fluxes (dashed contours), while the later response has preferentially southeastward propagation and positive zonal momentum fluxes (solid contours). In all cases, the dominant responses at the higher altitudes are largely dictated by turning levels due to strong winds opposite to GW propagation in the LT. At all times, however, GWs having high phase speeds are found to propagate in a range of directions, depending on the local winds.

Many more GWs succeeded in penetrating from convective sources into the MLT, and many of these were easily seen in the various airglow emissions measured at our three SpreadFEx optical measurement sites. These sites were typically east of the major convection, so the predominant eastward propagation appears to be consistent with primarily convective sources. Examples of GW propagation in the east-west plane are shown with Keograms of OH airglow brightness from Brasilia and Cariri in the lower panels of Fig. 5. Horizontal wavelengths were typically in the range ∼20 to 400 km, with the largest brightness variations occurring at intermediate scales of ∼50 to 200 km. While not displayed here, ray tracing of GWs having these horizontal scales, but lower frequencies than those penetrating into the TI, suggest largely eastward propagation and typical propagation times of several hours from their convective sources to the MLT. These results are generally consistent with the scales and largely eastward propagation seen in Fig. 5. Based on these observations and the accompanying ray tracing, we must be careful in attempting to link GWs in the MLT with plasma instabilities and bubbles at higher altitudes, as what dominates the airglow brightness modulations may not fully characterize the GWs that survive to 200 km and above. More quantitative and complete assessments of GW sources, generation, and spatial scales attaining MLT and higher altitudes are provided by Taylor *et al.* (2008), Takahashi *et al.* (2008), Vadas *et al.* (2008), Vadas and Fritts (2008), Fritts and Vadas (2008), and Fritts *et al.* (2008b) in our SpreadFEx special issue.

4.1.3 Bores in the MLT While not a central focus of the SpreadFEx measurement campaigns, our airglow, radar, and related satellite measurements also provided sensitivity to mesospheric bores occurring at MLT altitudes and to the wind and temperature fields in which they occurred. As bores are believed to be excited by GW instabilities, dissipation, and/or mean-flow interactions, their study represents an interesting extension of our campaign objectives and specific GW studies, and it benefits significantly from our comprehensive SpreadFEx data set. One example of a bore seen at Cariri on 1 October is shown in Fig. 6 at two times separated by 20 min. This bore structure was most visible in the OI 5577 Å emission, propagated towards the NE, and had an initial wavelength that appeared to shorten and a number of crests that appeared to increase over the 20-min interval displayed. Analysis of this event suggests a complex ducting structure (Fechine *et al.*, 2008) and helped motivate our initial modeling studies of bore excitation and evolution in thermal and Doppler ducts.

Bore structures, evolutions, and excitation have been studied previously by Dewan and Picard (1998, 2001), Seyler (2005), Fechine *et al.* (2005), and Medeiros *et al.* (2005), largely in highly idealized flows. Observed bores, however, occur in more complex environments in which both temperature and wind fields play a role in defining the ducting environment. In general, the separate contributions of temperature and winds (yielding Doppler ducts) do not occur at the same altitudes and are expected to impact bore (and linear ducted responses) differently, depending on propagation direction. To illustrate some of the variability

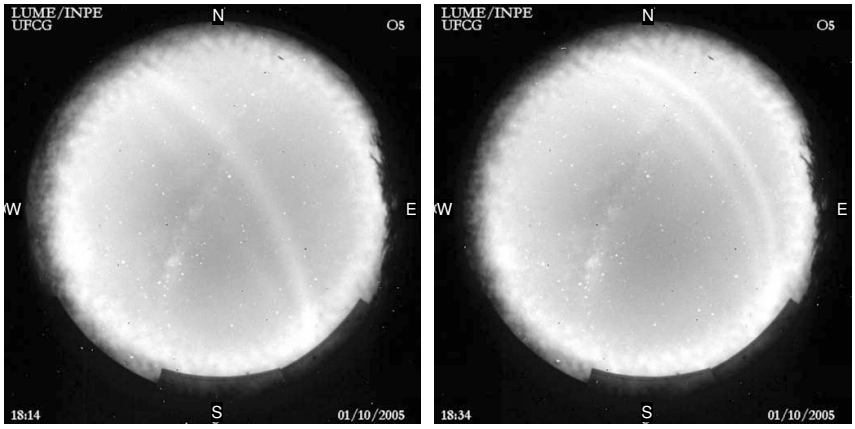

Fig. 6. A bore seen in OI 5577 Å emissions at Cariri on 1 October 2005 at times of 18:14 and 18:34 LT. The bore was less distinct in OH emissions, propagated towards the NE (upper right), and exhibited dispersion and an increasing number of wave crests in only 20 min.

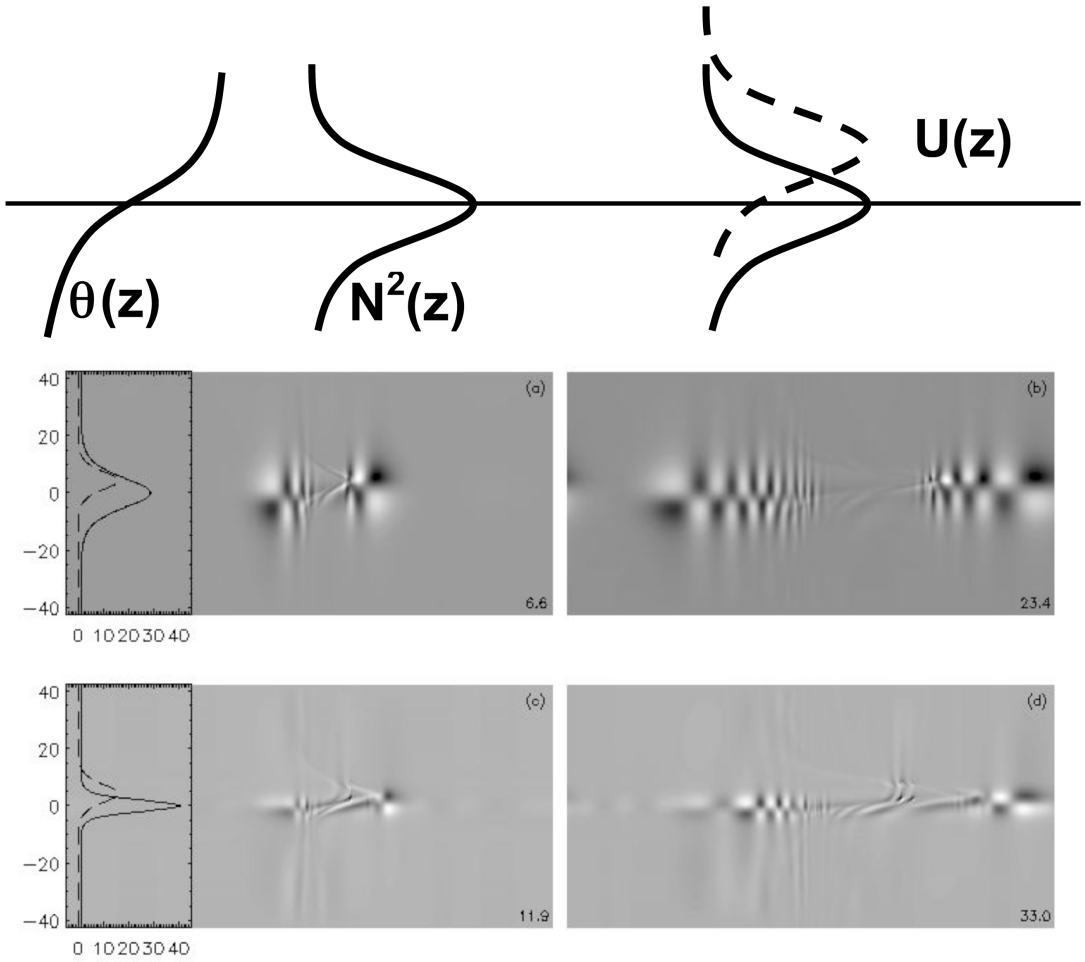

Fig. 7. Potential temperature and velocity profiles leading to ducting and enabling bore development and propagation (top). A sharp increase in potential temperature yields a local maximum in buoyancy frequency squared, $N^2(z)$; the profiles at top right show displaced thermal and Doppler ducts, which often accompany mean and low-frequency GW structures in the MLT. Lower panels show perturbation potential temperature fields exhibiting responses to horizontal Gaussian impulses for overlapping thermal and Doppler ducts when they overlap more fully (middle) and to a smaller degree (bottom). Shown are N^2 and velocity profiles (solid and dashed, respectively), with a peak $N^2 \sim 28$ and 40 times the background (top and bottom, respectively), a background $N = 0.01047$ s^{-1} (a buoyancy period of 10 min), thermal ducts of 8 and 3 km FWHM (top and bottom), Doppler ducts of 5 km FWHM (both), and a velocity maximum of $\sim$100 m s^{-1}. The Gaussian horizontal impulse had a maximum of $\sim$8 m s^{-1} and a FWHM of 5 km. The times (lower right in each panel) are in buoyancy periods following the impulsive forcing.

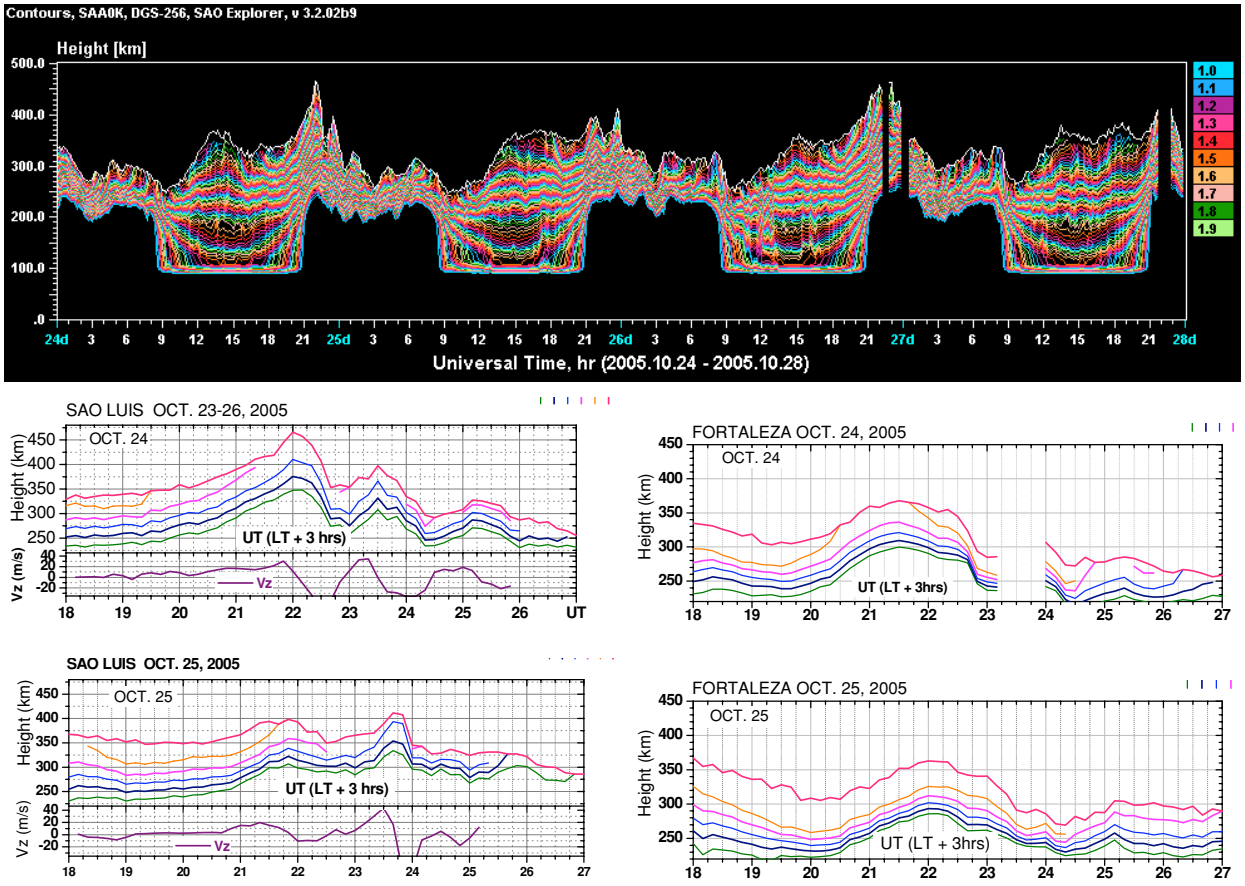

Fig. 8. Digisonde measurements at São Luis for 24 to 27 October 2005 (upper panel) and expanded versions of these data (from 1800 to 0300 UT) for São Luis (lower left) and Fortaleza (lower right) for the first two of these nights. Inferred vertical velocities are shown on the bottom of the displays at São Luis for each night.

accompanying both thermal and Doppler ducts, we show two responses arising for $\mathrm{sech}^2(z/h)$ Doppler and thermal ducts of different depths and displaced by half the FWHM of the Doppler duct in the vertical in the middle and lower panels of Fig. 7. In these examples, we assumed a FWHM of the Doppler duct of 5 km, a Doppler duct jet maximum of $\sim$100 m s^{-1}, thermal duct FWHM of 8 and 3 km (top and bottom images in Fig. 8), a background $N = 0.01047$ s^{-1} (a buoyancy period of 10 min) in both cases, and thermal duct maxima of $N = 0.056$ and 0.066 s^{-1}, respectively. Both ducting environments were excited with a 2D horizontal Gaussian impulse of maximum velocity $\sim$8 m s^{-1} and FWHM of 5 km centered at the thermal duct.

For the broad thermal duct (middle panels of Fig. 7), there are two distinct ducted features, one occurring somewhat below the thermal duct propagating to the left and a second somewhat above the thermal duct propagating to the right. Each feature exhibits a largely anti-symmetric response in the temperature (and vertical velocity) field because of the symmetric horizontal forcing and normal dispersion, with the larger wavelengths having larger phase and group velocities than the smaller wavelengths. The larger and smaller wavelengths within each response are also centered at somewhat different altitudes. This is because the mean velocity varies across the thermal duct, and smaller-scale motions having smaller phase speeds are more influenced by mean winds and tend to occur nearer the maximum velocity in their direction of propagation. In fact, the larger wavelength ducts are defined more by the thermal structure, and the smaller wavelength ducts are defined more by the wind structure.

The lower panels in Fig. 7 shows the response when the thermal duct is both narrower (3 rather than 8 km) and stronger (a peak $N^2 \sim 40$ times, rather than $\sim$28 times, the background). Both responses in this case are much more confined about the thermal duct, and there is now very different dispersion between the left- and right-propagating modes. The left-propagating packet closely resembles that in the upper panels, except that it is shallower. The right-propagating response, however, is both shallower and exhibits apparently different dispersion for the larger and smaller wavelengths. The larger wavelengths propagate near the thermal duct as before, but the smaller wavelengths now appear to comprise a distinct wave packet having a much smaller group velocity and occurring near the peak of the Doppler duct rather than the thermal duct. Indeed, it appears possible that the two parts of this response are exhibiting different responses due to anomalous dispersion expected in a dual-ducting environment (Fritts and Yuan, 1989). These features will be explored in greater detail elsewhere in this, and the SpreadFEx, special issues (Fechine *et al.*, 2008; Laughman *et al.*, 2008).

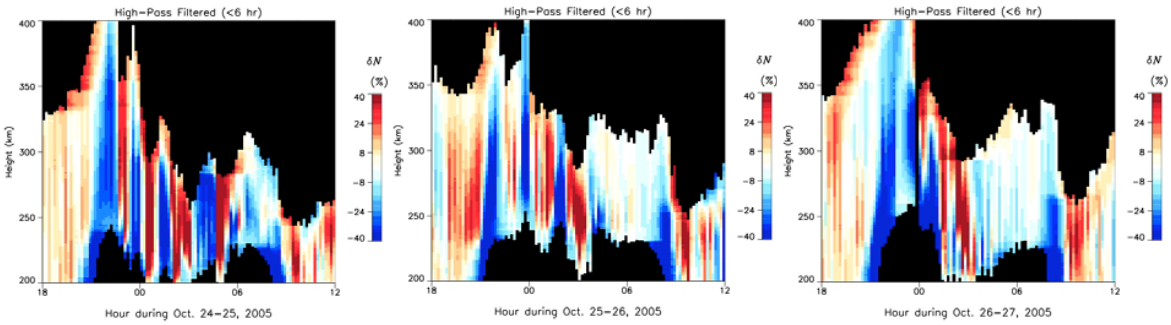

Fig. 9. Electron density fluctuations computed from the digisonde data for all three nights from 1800 to 1200 UT. Note the large electron density fluctuations (up to ∼40%), with oscillation periods of ∼20 min to 2 hr and apparent downward phase progressions at altitudes of ∼280 km and below. Note that large K_p values (∼4) occurred only on 25 October, with smaller values the following days.

4.2 Electron densities, TEC, and GWs in the *F* layer

We now turn to an overview of the observational evidence of possible neutral and plasma coupling at the bottomside *F* layer obtained during the SpreadFEx measurement campaigns. Digisonde measurements at São Luis for 24 to 27 October 2005 are shown for reference in the upper panel of Fig. 8. Expanded versions of these data (18 to 03 UT), and the corresponding data from Fortaleza, are shown for the first two of these nights (24/25 and 25/26 October) in the middle and lower panels, respectively. Electron density fluctuations computed from the digisonde data from São Luis for all three nights from 1800 to 1200 UT are shown in Fig. 9. These perturbations appear larger than often observed elsewhere, but are indicative of the potential for large plasma density perturbations in the *F* layer, though the specific roles of these perturbations in generating ESF and plasma bubbles are unclear at this time.

Each night exhibits the expected rise in the *F* layer accompanying the PRE and a series of oscillations thereafter having large amplitudes and apparent vertical displacements. Observed periods range from ∼20 min to 2 hr, with the largest electron density fluctuations (∼40%) occurring at the longer periods. Also seen are apparent downward phase progressions, especially at altitudes of ∼280 km and below. These are most apparent in the electron density fluctuations at the longer periods from ∼00 to 04 UT for each day shown in Fig. 9. There are also several regions in each panel where opposite phases of the perturbation overlap each other. This provides some indication of apparent GW vertical wavelengths. More quantitative estimates of GW amplitudes, scales, and likely propagation conditions inferred from these data are discussed in Section 5 below.

Prompt penetration electric fields have been suggested to lead to strong uplift of the *F* layer (Abdu *et al.*, 2003; Huang *et al.*, 2004) and are expected to occur on a global scale (Kelley, 1989). Substorms may likewise contribute significant short-term perturbations at equatorial latitudes. Such effects are expected to be more pronounced under enhanced high latitude convection conditions, so we display the K_p index during September and October 2005 in Fig. 10. These data reveal significant K_p (∼4 from 00 to 12 UT) the evening of 24/25 October, but with substantially smaller values of ∼2 the next two nights. The D_{st} index, which is available at significantly higher temporal resolution, was likewise relatively quiescent, with mean values for 24 to 27 October of +1, −20, −21, and −15, with peak negative values of −39, −33, and −23 the last three days. ACE/MAG magnetic fields during these days were similarly weak to moderate. Thus, apart from the evening of 24/25 October, with a mean $K_p \sim 4$ and a mean D_{st} of −20 nT, there is little evidence that there were significant geomagnetic influences. And even on this night, D_{st} values were substantially smaller than −100 nT, and are thus relatively geo-magnetically quiet.

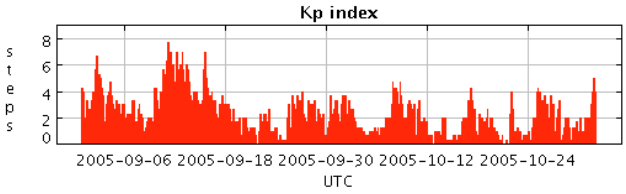

Fig. 10. K_p index during September and October 2005. Tabular data yield mean values of 1, 3.5, 2.5, and <2 for 24 to 27 October, respectively, averaged in UT.

Evidence of GWs at even higher altitudes is obtained from GPS estimates of the temporal derivative of integrated or total electron content (IEC or TEC), assumed to be representative of changes at the altitudes of maximum electron density, or sub-ionospheric point (SIP), ∼300–400 km, by the use of various GPS receivers in Brazil. Examples of such information as derived from data obtained with the GPS receiver at Fortaleza on 24 October are shown in Fig. 11 which suggest typical GW periods at these altitudes of ∼15 to 60 min. The various satellites viewed by the receiver during these times indicate similar temporal variations at the same times, suggesting spatial coherence among the various "piercing points" of the ionosphere. For reference, the vertical dashed red line in Fig. 11 indicates the anticipated start time for plasma bubble initiation (Woodman and LaHoz, 1976), suggesting that the $d(\mathrm{TEC})/dt$ fluctuations seen at earlier times must be due to GW influences in the ionosphere rather than plasma bubbles themselves. These data are challenging to interpret unambiguously, however, because it is difficult to separate temporal variations that may be due to GW propagation from possi-

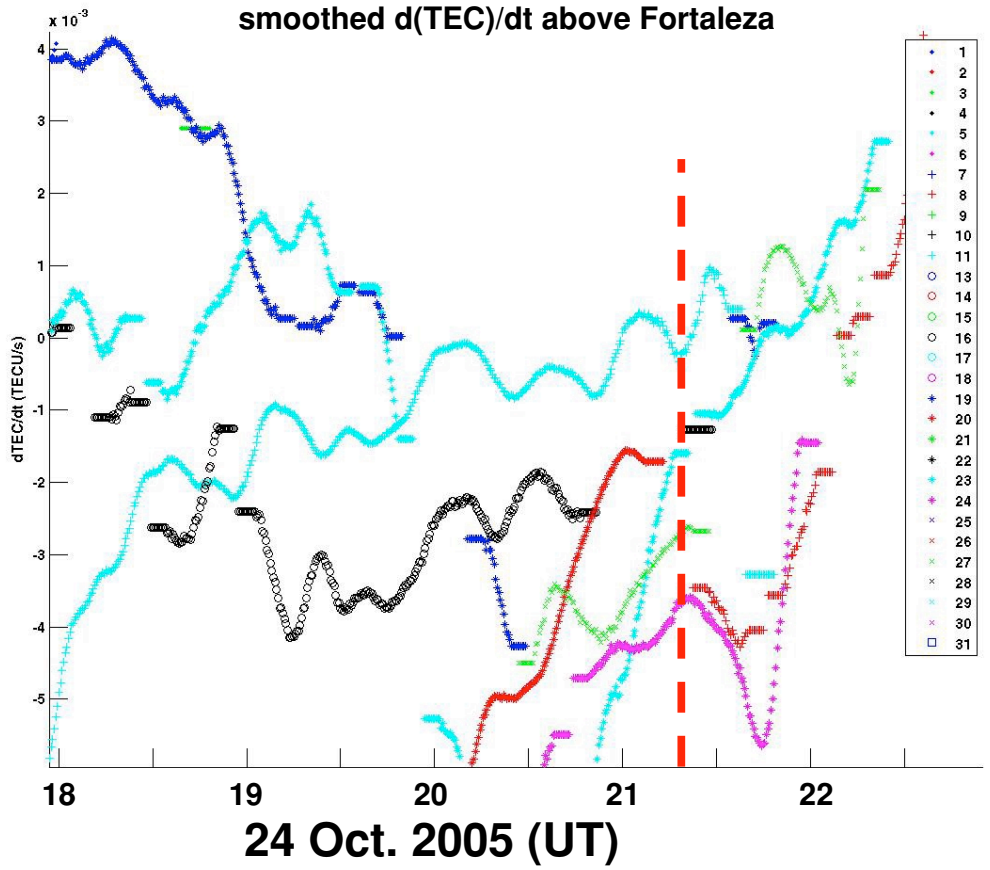

Fig. 11. Time series of $d(\mathrm{TEC})/dt$ for eight GPS satellite traverses observed from Fortaleza during 24/25 October 2005 and coincident with the left perturbation electron density plot in Fig. 9. Note that most oscillations have apparent periods of ∼20 min to 1 hr and that oscillations are apparent well before spread *F* onset, shown approximately by the dashed red line.

ble spatial variations accompanying slow satellite motion. Nevertheless, they demonstrate fairly persuasively that GW perturbations in electron density also extend to higher altitudes than implied unambiguously by the digisonde electron densities.

To increase the potential for the detection of GWs and small-scale plasma structures in the ionosphere during SpreadFEx, five temporary GPS stations with an approximate spacing of 50 km between sites were also installed near the imager site in central Brazil at Fazenda Isabel, São João de Aliança (FAZ1), Parque Nacional, Alto Paraiso (ALPA), Ibama, Alvorado do Norte (ALVO), Flores de Goias (FLOR), and Teresina de Goias (TERE). The locations of each of these systems, along with permanent sites at Brasilia (BRAZ), Montes Ciaros (MCLA), and Uberlandia (UBER) from the Rede Brasileira de Monitoramento Contínuo (RBMC) GPS network surrounding the temporary GPS stations, are listed in Table 2. For these systems, the integrated electron content (IEC) was calculated from dual-frequency carrier phase observations (Lanyi and Roth, 1988; Hofmann-Wellenhof, 1994; Calais and Minster, 1998), with a 4th-order polynomial removed from each IEC time series to remove the effects of the diurnal variation in electron content. Array processing techniques developed to detect propagating disturbances in dual-frequency GPS time series (Calais *et al.*, 2003) are currently being used to characterize signals observed by this small array.

Table 2. Locations of the GPS sites in central Brazil employed for SpreadFEx.

Name	Latitude	Longitude
ALPA	−14.073832	−47.788579
ALVO	−14.406658	−46.506171
FAZ1	−14.665781	−47.602838
FLOR	−14.49657	−47.034927
TERE	−13.696128	−47.264411
BRAZ	−15.93	−47.86
MCLA	−16.71	−43.86
UBER	−18.89	−48.31

Detrended IEC time series are shown for the three sites, ALPA, TERE, FAZ1, for the night of days 274/275 (1/2 October 2005) in Fig. 12(a), (b), and (c). Depletions in the IEC are clearly seen as troughs in the time series from all satellites that had tracks to the west of the array (PRN28, PRN4, and PRN8). Figure 12(d) shows a map of the location of the SIP at each time sample of the time series, with the color indicating the magnitude of the IEC. Blue color indicates points where the IEC dropped sharply. This happened more or less simultaneously for points from ALPA and FAZ1 to PRN28 and at a later time for station TERE.

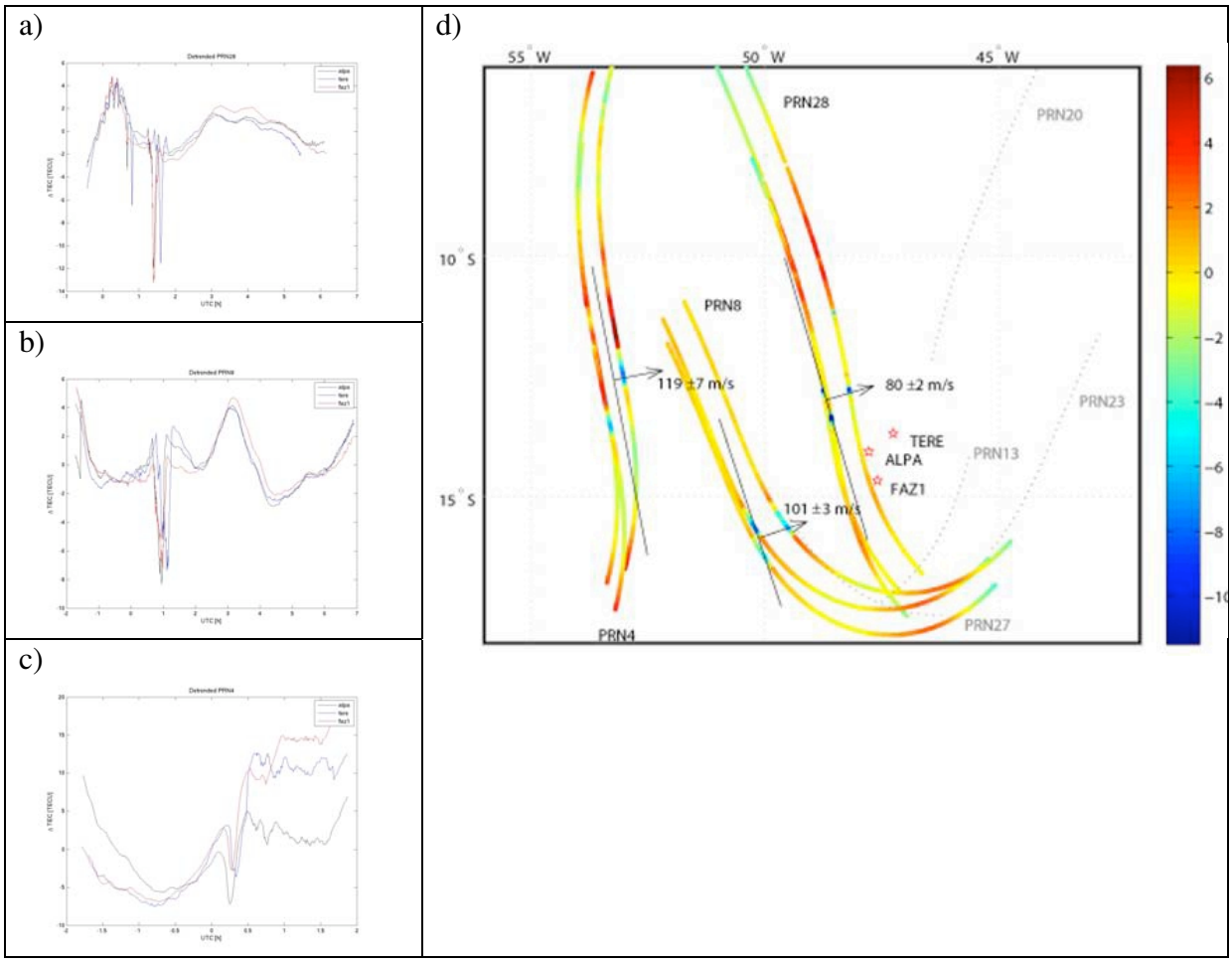

Fig. 12. (a) Detrended IEC time series for satellite PRN28 recorded at stations ALPA, TERE, FAZ1. Two troughs are seen at about 00:45 UTC and 01:30 UTC on 2 Oct 2005. (b) Detrended IEC time series for satellite PRN8. (c) Detrended IEC time series for satellite PRN4. (d) Map showing the traces of the subionospheric points for each satellite, with traces from PRN4 furthest west, PRN8 in the center, and PRN 28 furthest east. Low amplitude of IEC in the detrended signal is shown in blue color. The perturbation is assumed to propagate perpendicular to the line spanned by the simultaneous troughs at ALPA and FAZ1 reaching TERE at a later time. Approximate propagation speeds are shown that have been derived from data from each satellite. The location of the three GPS sites is indicated with red stars.

Assuming a disturbance propagating perpendicular to a line through ALPA and FAZ1 that reached the SIP from TERE at a later time, a propagation speed of ∼80 m s^{-1} in a direction roughly ENE was inferred. Similarly, for PRN8 the propagation direction was approximately eastward at ∼101 m s^{-1}, while traces from PRN4 showed eastward propagation at ∼119 m s^{-1}. Indeed, the inferred propagation directions and speeds, as well as their variations with longitude and decreases with time, agree with similar estimates using airglow imagers (see Fig. 5). Future analysis will attempt to estimate vertical motions by combining SpreadFEx GPS and airglow data.

4.3 Spread *F* and plasma bubble occurrence, structure, and correlations

The evolution of the bottomside *F* layer into plasma bubbles extending to higher altitudes is illustrated in Fig. 13 with VHF radar RTI plots at São Luis for the nights of 24/25 and 25/26 October 2005. These data correspond to the first two nights of digisonde data and electron density fluctuations shown in Figs. 8 and 9. The RTI plots indicate the presence of ESF at the bottomside *F* layer beginning as low as ∼230 to 250 km in most cases, with apparent backscatter also occurring on 24/25 October as low as ∼200 km beginning just before 00 UT. Plasma bubbles appear not to be initiated until the bottomside *F* layer is elevated to altitudes of ∼250 to 300 km. We must be careful in our interpretation of these data, however, as plumes that are first observed at higher altitudes were necessarily seeded at earlier times to the west of São Luis.

Closer examination of Fig. 13 (top panel) suggests that ESF and RTI lead to bubble generation accompanying the strong upward motions of the bottomside *F* layer at ∼22 UT and just before 00 UT on 24/25 October that are also seen in the digisonde data of electron density fluctuations in Figs. 8 and 9. The periodicity of the plasma bubble generation appears consistent with the lower-frequency modulations (∼2-hr periods) in these other data sets that were suggested to indicate possible GW influences below ∼280 km. It is more difficult to estimate the time of initiation of the second plasma bubble, however, because the bubble had already penetrated to high altitudes at the time of its detection over São Luis. It is also not possible to assess the spatial scales or temporal evolutions of these bubbles from the RTI plots alone. Indeed, these data highlight

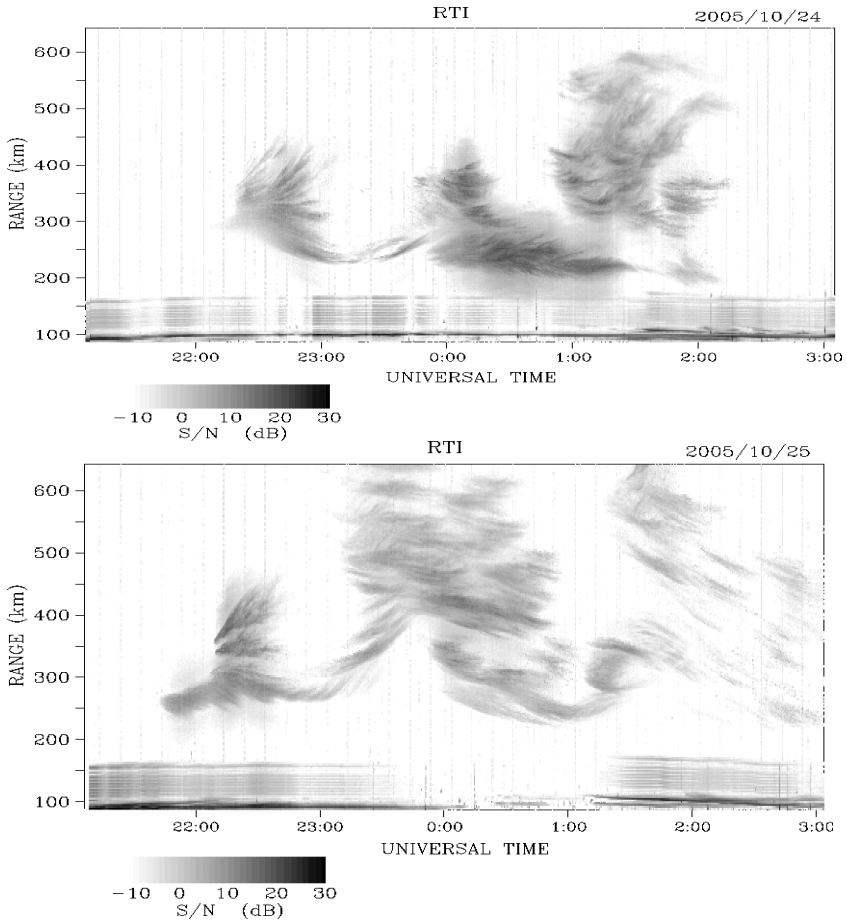

Fig. 13. Spread *F* and plasma bubbles observed on 24/25 (top) and 25/26 October (bottom) by the VHF radar at São Luis during the SpreadFEx measurement campaign. The plume occurrence on both days follows closely the uplifted bottomside *F* layer seen in Figs. 8 and 9 and exhibits a similar periodicity.

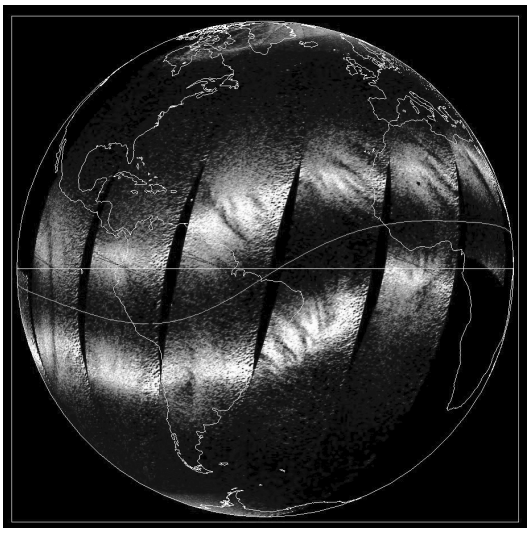

Fig. 14. TIMED/GUVI 1356 Å emissions on successive orbits during the SpreadFEx campaign. Dark bands are field-aligned and vertically-integrated plasma depletions.

a challenge in interpreting our ground-based plasma bubble measurements, as the RTI plots display a mixture of spatial structures and temporal variability.

Shorter period fluctuations (∼30 min) also seen in the electron density data did not obviously make distinct contributions to plasma bubble seeding or spatial structure. To the extent that the ∼2-hr oscillations at lower altitudes are indicative of GW perturbations, these data suggest that neutral atmosphere GW motions may have played an important role in the seeding process. The same periodicities were also present at the bottomside *F* layer on 25/26 October (Figs. 8, 9, and 13, bottom, center, and bottom panels), and the longer periods (∼2 hr) again appear to correlate well with the vertical plasma motion at these altitudes. In this case, shorter periods were more prevalent in the digisonde and electron density data and may have played a larger role in seeding the apparently more complex bubble structures at higher altitudes. Again, however, it appears difficult to establish a clear correlation between fluctuations at the bottomside *F* layer and the plasma bubbles observed at higher altitudes after the initial bubble occurrence because the later bubbles were already fully developed when observed over São Luis. The potential for GWs present at the bottomside *F* layer to contribute to plasma instability seeding and growth rates is explored in greater detail below.

To resolve ambiguities in the interpretation of RTI plots from the VHF radar, additional data sets or analysis methods are required. Fortunately, the SpreadFEx campaign benefits from several. Airglow measurements at 6300 Å such as displayed in Keograms in the upper panels of

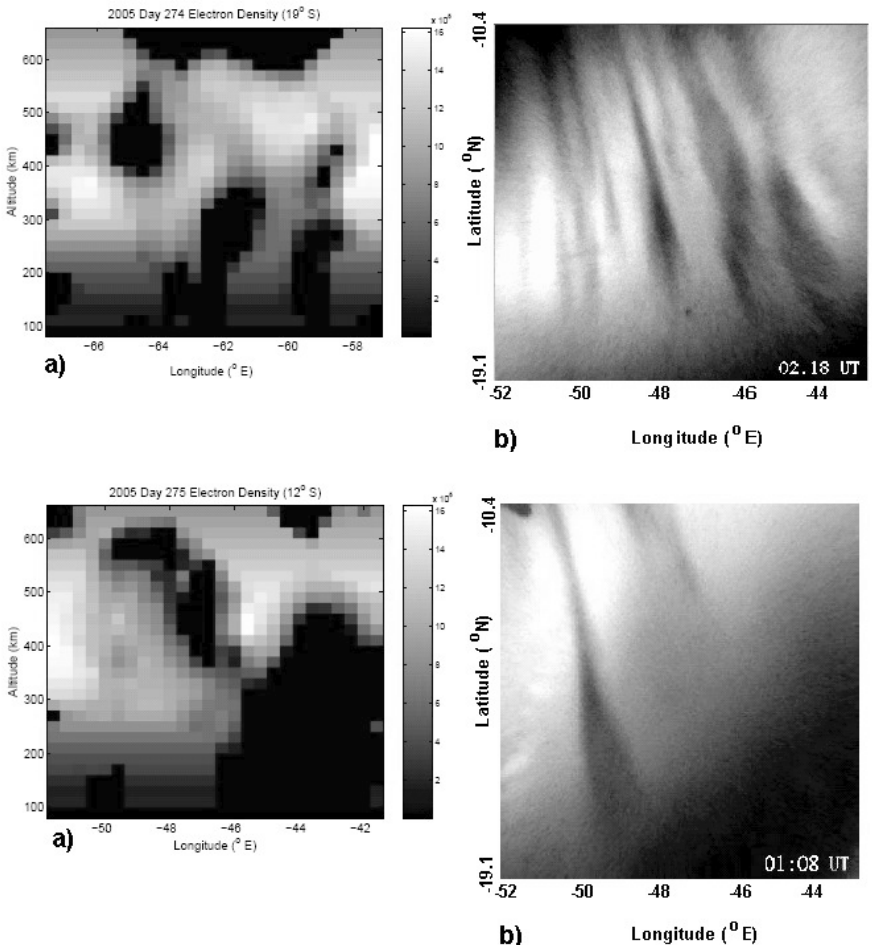

Fig. 15. Vertical cross-sections (left) of plasma depletions at 19°S (top) and 12°S (bottom) from tomographic inversions of GUVI 1356 Å emissions (left) and corresponding 6300 Å emissions at Cariri (right) for 1 and 2 October (days 274 and 275), respectively. Note that the images were not coincident in longitude on day 274, but were on day 275.

Fig. 5, provide information on spatial scales and drift speeds. These suggest typical plume separations of ∼100 to 500 km, at least at the altitudes that contribute most to plasma depletions, will play an important role in our more quantitative analyses to follow. Additional information on plasma bubble geometries and evolutions can be obtained by interferometric analysis of the VHF radar data (Hysell, 1996), but these results will likewise await our SpreadFEx special issue. Finally, data from the GUVI instrument aboard the TIMED satellite will be seen below to yield a dramatic enhancement of our ability to quantify plasma bubble structures via tomographic inversions of 1356 Å emissions at the times of these overpasses.

4.4 Plasma bubble structures inferred from space

The GUVI instrument aboard the TIMED satellite provides another valuable data set for plasma bubble studies, and there were several overpasses that were coincident in space and time with some of our SpreadFEx measurements. The primary measure of bubble structures by GUVI is via the 1356 Å emissions, which show significant line-of-sight depletions when viewing bubbles near nadir. An example of the bubbles seen by GUVI over S. America during our SpreadFEx measurements is shown in Fig. 14. These data afford another opportunity to correlate bubble structures with 6300 Å airglow images and VHF radar RTI plots in defining bubble scales and morphology.

Even more exciting is the ability to perform tomographic inversions with the GUVI data because the satellite motion and GUVI viewing have components normal to the magnetic field over Brazil. This allows extraction of electron density measurements in a plane normal to the field lines having horizontal and vertical resolution of ∼40 and 20 km, respectively. This allows for unprecedented resolution of the spatial scales of individual bubbles and much more quantitative comparisons with our SpreadFEx correlative data than would otherwise be possible. Two examples of these data from 1 and 2 October and the corresponding 6300 Å airglow images from Cariri viewing the same bubble structures are shown in Fig. 15. While we did not perform an extensive analysis of these correlative data prior to writing this paper, this is the focus of the effort by Kamalabadi *et al.* (2008) in the SpeadFEx special issue.

5. Potential Neutral Atmosphere Contributions to ESF, RTI, and Plasma Bubble Seeding

The RTI and ESF preconditioning growth rates expressed through Eqs. (1) and (2) in Section 2.2 above indicate the expected sensitivities of these plasma instabilities to neutral motions able to impact these quantities. Here we examine the potential direct contributions of such neutral atmo-

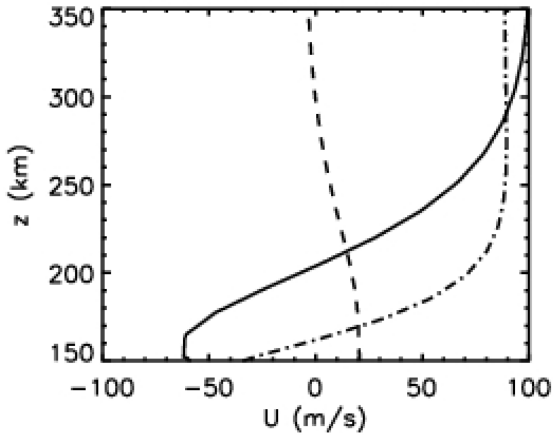

Fig. 16. Zonal tidal winds on 25/26 October 2005 at 55°W, 12.5°S over Brazil at 21 (dashed), 00 (solid), and 03 UT (dash-dotted) for a TIME GCM model run spanning the SpreadFEx campaign period and initialized with the global NCEP reanalysis for this period.

sphere motions to plasma instabilities accompanying neutral wave perturbations occurring at *F* layer altitudes. An assessment of possible GW influences at lower altitudes that map electric field or other perturbations to higher altitudes is more complex and beyond the scope of this summary of first SpreadFEx results. For more complete discussions of related SpreadFEx analyses, we refer the interested reader to Fritts *et al.* (2008a, b), Abdu *et al.* (2008), Kherani *et al.* (2008), and other papers in the SpreadFEx special issue.

5.1 Tidal influences at the bottomside *F* layer

A major contributor to TI structure that appears to have obvious relevance to the preconditioning arguments of Kudeki *et al.* (2007) is the neutral atmosphere tidal structure that penetrates to high altitudes, and is generated in situ, at equatorial latitudes. The migrating tides are expected to comprise the dominant motion field at *F* layer altitudes, and their temporal behavior described by the TIME GCM appears to make a clear contribution to the potential plasma instability processes envisioned by these authors (we note, however, that the TIME GCM tidal structures at *F* layer altitudes have yet to be validated, so their detailed amplitude and phase structures should be considered to be only suggestive at this time). Zonal tidal winds on 25/26 October 2005 over the dip equator in Brazil at 21, 00, and 03 UT for a model run spanning the SpreadFEx campaign period are shown in Fig. 16. These profiles suggest that zonal winds are small or negative (westward) at ∼21 UT and swing sharply positive (eastward) thereafter at *F* layer altitudes, which appears to correlate well with onset times for plasma bubbles noted by previous authors. If the dependence of ESF initial instability is indeed a strong function of eastward winds, as argued by Kudeki *et al.* (2007), then it seems likely that tidal winds will play a very large role in determining when strong instability is possible, or at the least, in modulating instability growth rates. Because tidal structures exhibit significant amplitude variability at lower altitudes, due both to variable forcing in the lower atmosphere and modulation of processes coupling to higher altitudes, they are also expected to impose this variability on ESF, RTI, and plasma bubble occurrence statistics at *F* layer and higher altitudes. A similar suggestion was voiced by Meriwether *et al.* (2008) based on long-term Fabry Perot interferometer measurements in Peru. Indeed, solar-cycle variations in thermospheric temperatures will also modulate tidal amplitudes and phases and could contribute, together with the modulation of GW penetration altitudes in the TI, to the solar-cycle occurrence statistics of plasma bubbles.

5.2 GW perturbations at the bottomside *F* layer

GW motions were suggested above to contribute to bottomside *F* layer electron density fluctuations and to corresponding neutral atmosphere wind and temperature perturbations and displacements. Here we attempt to estimate the magnitudes of these fluctuations in order to assess their potential to contribute to the plasma instability processes discussed above. To assign the most conducive GW geometry, we consider the idealized plasma instability environment envisioned by Hysell *et al.* (2004) shown in Fig. 17. This schematic, and the arguments by Kudeki *et al.* (2007), suggest that instability will be favored for perturbations that enhance both electron density gradients and neutral-minus-plasma zonal motions ($U_n - U_p$) in regions where the plasma has been elevated. This is the lower left quadrant of the clockwise circular plasma motion depicted in Fig. 17, where the plasma motion opposes the neutral motion and induces rising motion westward and above, which increases the perturbation displacements. As we will see below, GWs can enhance eastward motions accompanying either upward or downward motions, but enhanced neutral and plasma density gradients always accompany downward neutral motions.

Considering first the neutral GW perturbations implied by a given fractional electron density gradient, we assume mean neutral and electron density profiles of the form

$$\rho(z) = \rho e^{-z/H} \tag{3}$$

and

$$\rho_e(z) = \rho_e e^{z/H_e}, \tag{4}$$

where H and H_e are the respective (positive) neutral and electron density scale heights. We also assume GW velocity, pressure, potential temperature, and neutral density perturbations of the form

$$(u', v', w', p'/p, \theta'/\theta, \rho'/\rho) \sim \exp[i(kx + ly + mz - \omega t) + z/2H], \tag{5}$$

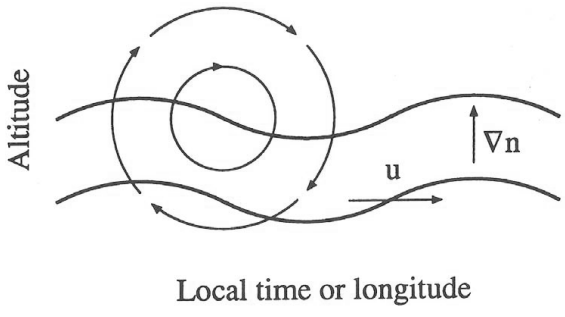

Fig. 17. Schematic of plasma instability growth geometry and its dependence on neutral wind and the plasma gradient (after Hysell *et al.*, 2004).

where primes denote perturbations and $\mathbf{k} = (k, l, m)$ is the GW wavenumber vector. Assuming that the plasma moves with the GW perturbation wind field and that there are no chemical or electrodynamic processes that also impact plasma densities, the electron (or ion) continuity equation, $d\rho_e/dt = 0$, may be written as

$$\rho_e'/\rho_e = ku'/\omega + lv'/\omega + mw'/\omega - iw'/\omega H_e. \quad (6)$$

Employing the energy conservation and continuity equations (Fritts and Alexander, 2003)

$$i\omega\theta'/\theta = \left(N^2/g\right) w' \quad (7)$$

and

$$i\omega\rho'/\rho = iku' + ilv' + (im - 1/2H)w'. \quad (8)$$

Assuming that motions are approximately hydrostatic such that $\theta'/\theta \approx -\rho'/\rho$ and employing the relation $N^2H/g + gH/c_s^2 = 1$ or $N^2 = (g/H)(1 - 1/\gamma)$, with $c_s^2 = \gamma gH$ and $\gamma = c_p/c_v = 1.4$, we obtain

$$\begin{aligned}\left(\rho_e'/\rho_e\right) / \left(\rho'/\rho\right) &= 1 - \left(g/N^2\right)\left(1/2H + 1/H_e\right) \\ &= -(2-\gamma)/2(\gamma-1) \\ &\quad -\gamma H/(\gamma-1)H_e. \end{aligned} \quad (9)$$

Finally, the GW polarization relations (Fritts and Alexander, 2003) yield relations for vertical and horizontal perturbation velocities in terms of fractional densities

$$w' \sim \left(g\omega/N^2\right)\rho'/\rho, \quad (10)$$

or in a form that is more commonly used

$$u_h' = -(m/k_h)\, w' \sim \left(m/k_h\right)\left(g\omega/N^2\right)\rho'/\rho = \beta(g/N)\rho'/\rho. \quad (11)$$

In the above, u_h' and w' are the horizontal and vertical GW perturbation velocities, $\omega = k_h(c - U_n)$ is the GW intrinsic frequency, $k_h = (k^2 + l^2)^{1/2} = 2\pi/\lambda_h$ and $m = 2\pi/\lambda_z$ are the GW horizontal and vertical wavenumbers, c and U_n are the GW horizontal phase speed and the neutral mean wind in the direction of propagation (assumed zonal in the discussion of plasma instabilities above), λ_h and λ_z are the GW horizontal and vertical wavelengths, and $\beta \sim (1 - \omega^2/N^2)^{1/2} \sim 1$ for hydrostatic and small-scale GWs. With our degree of approximation, Eq. (10) is accurate for all GWs in the TI, whereas $\beta \sim 1$ in Eq. (11) only when $\lambda_h^2 \ll 16\pi^2H^2$ and $\omega^2 \ll N^2$. These are reasonable assumptions at lower altitudes, but they are less accurate where GW vertical wavelengths exceed ~100 km and intrinsic frequencies exceed $\omega \sim N/3$, as we expect to occur in response to increasing kinematic viscosity and thermal diffusivity in the TI (Vadas and Fritts, 2005, 2006; Vadas, 2007; Fritts and Vadas, 2008). When $\omega > N/1.4$ and GW scales increase, $\beta < 1/2$ and approximations appropriate for the lower atmosphere lead to overestimates of u_h' based on density measurements. We again note that we have considered only advective effects in the above discussion, and have specifically neglected chemical, electrodynamic, and magnetic influences on plasma densities hat may be competitive. Thus, plasma perturbations will almost certainly be smaller than suggested by the above equations.

Under solar minimum conditions, thermospheric temperatures above ~200 km are ~600 K and gradients are small, such that $N \sim 10^{-2}$ s^{-1} and the buoyancy period is $T_b \sim 10$ min. Thus we should expect typical GW intrinsic periods of $T_i = 2\pi/\omega \sim 30$ min (Vadas, 2007; Fritts and Vadas, 2008), and the GWs suggested by the electron density and TEC fluctuations discussed above are in the expected range. We also expect neutral and electron density scale heights of $H \sim 15$ to 20 km and $H_e \sim 20$ to 50 km, such that the ratio of fractional electron to neutral density fluctuations is likely something less than $(\rho_e'/\rho_{e0})/(\rho'/\rho_0) \sim 5$ or smaller. The 10 to 40% electron density fluctuations inferred from the digisonde data then imply horizontal and vertical GW perturbation velocities of $u' \sim 10$ to 40 m s^{-1} and $w' \sim 3$ to 10 m s^{-1} (or larger, if electron density fluctuations are under-estimated) if motions occurred at smaller scales and nominal intrinsic frequencies of $\omega \sim N/3$, with estimates for u' ~ 2 times smaller for higher frequencies and larger scales. Thus, the velocity perturbations of GWs believed to have been present in the bottomside *F* layer during plasma bubble seeding during the SpreadFEx measurements appear to have been sufficiently large to impact plasma instability growth rates if they existed in the relevant regions and induced the appropriate perturbations to the differential plasma and neutral zonal velocities and/or the length scale (H_e) of the electron density gradient. As suggested above, GWs also contribute to perturbations of the mean electron density gradient and may thus contribute to modulation of plasma instability growth rates through both differential neutral and plasma motions and enhanced electron density gradients.

5.3 GW impacts on plasma growth rates

We now consider the GW orientations and structures implied by our SpreadFEx measurements and their possible contributions to plasma instabilities and growth rates, with a focus on direct influences at the bottomside *F* layer. Our SpreadFEx airglow observations and our limited ray tracing of GWs from convective plumes to date imply a preference for approximately zonal GW propagation in the MLT, though this may simply be a consequence of our SpreadFEx observations occurring generally to the east of the most intense convection. The TIME GCM simulation results employed here imply strong zonal and meridional tidal winds (and associated GW filtering) exhibiting significant spatial (in altitude and latitude) and temporal variability at the bottomside *F* layer. However, the tendency for eastward tidal winds to arise in the early evening hours appears to be consistent with the needed orientation of neutral atmosphere perturbations potentially contributing to RTI seeding and plasma bubble generation. This also implies preferential westward GW propagation at these altitudes, though weaker winds at lower altitudes would allow more isotropic GW propagation.

Assuming first that ρ_e' rather than ρ_e'/ρ_{e0} is constant with altitude, because of the apparent maxima of the latter between ~250 and 300 km and the apparent decrease above, we can express the local electron density gradient as (again assuming only advective effects)

$$\frac{\partial\rho_e}{\partial z} = \frac{\partial}{\partial z}\left(\rho_{e0} + \rho_e'\right) = \frac{\rho_{e0}}{H_e} + \frac{\partial}{\partial z}\left[\rho_e' \exp(imz)\right]$$

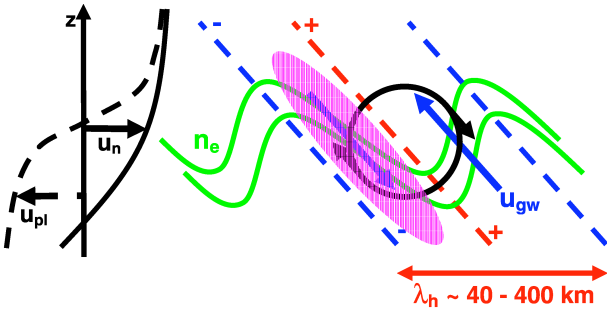

Fig. 18. Profiles of zonal neutral wind (U_n, solid) and plasma motion (U_{pl}, dashed) in the bottomside *F* layer (left) expected under ESF and RTI seeding conditions. At right are shown surfaces of constant neutral and electron densities (green, assuming neutral advection) due to an upward- and westward-propagating GW with maximum upward and downward displacements (blue and red dashed lines) regions of minimum and maximum neutral and electron densities, respectively. Neutral zonal and vertical winds are shown with blue arrows, the black circle shows the expected plasma motion (Hysell *et al*., 2004), and the pink region shows where neutral GW motions oppose horizontal and vertical plasma motions (contributing to polarization electric fields) and enhance the vertical electron density gradient, all of which enhance the expected plasma instability growth rates anticipated by Kudeki *et al*. (2007).

$$= \rho_{e0}\left[\frac{1}{H_e} + \frac{\rho_e'}{\rho_{e0}} im \exp(imz)\right]. \quad (12)$$

The ratio of perturbation to mean contributions is then $\sim(\rho_e'/\rho_{e0})mH_e$ within the phase of the GW having the largest positive gradient. For a GW with a vertical wavelength of $\lambda_z \sim 100$ km, which is consistent with apparent vertical structure in the electron density fluctuations seen in Fig. 9 and with expectations of assessments of GW wavelength variations due to increasing kinematic viscosity in the TI (Vadas and Fritts, 2006; Vadas, 2007; Fritts and Vadas, 2008), this ratio maximum is

$$\frac{\rho_e'}{\rho_{e0}} mH_e \sim 0.5 \text{ to } 1 \quad (13)$$

for the ranges of reasonable GW amplitudes, wavelengths, and plasma scale heights H_e anticipated at the bottomside *F* layer.

We are now in a position to assess how the various GW perturbations of horizontal and vertical winds and plasma density gradients may impact the plasma growth rates discussed above (with the above caveats about the neglect of chemical and electrodynamics effects). We begin by summarizing the mean structure of the neutral thermosphere and ionosphere anticipated to yield significant plasma growth rates by Kudeki *et al*. (2007). These conditions are shown in the left panel of Fig. 18. The important features appear to be 1) an eastward neutral wind at higher altitudes (due largely to tidal motions that only become significantly eastward at the time of observed plasma bubble formation), 2) a westward plasma motion partially decoupled from the neutral motions at the bottomside *F* layer, and 3) a strong vertical plasma (and electron density) gradient at the same altitudes. Considering GW influences on both neutral winds and electron density and plasma gradients, there are two possible GW orientations that imply different contributions to key terms in the instability growth rates. A GW having westward propagation and westward tilts of phase surfaces with altitude (as depicted in the right panel of Fig. 18) will provide the optimal enhancements of the important terms in the plasma growth rate suggested by Kudeki *et al*. (2007) in a common volume (or more likely in multiple similar volumes), specifically plasma density gradient and $(U_n - U_p)$ enhancements (see Eq. (2)). Westward-propagating GWs also have downward motions where eastward motions and electron density gradients are enhanced. But this is also considered to be beneficial for plasma instabilities, especially the RTI (Fejer, 1996).

Thus we assume an upward- and westward-propagating GW will contribute greater potential enhancements to the growth rate in Eq. (2) for the sake of this discussion. The right side of Fig. 18 shows surfaces of constant electron density (per unit mass, in green) for this GW orientation, with maximum upward and downward displacements (blue and red dashed lines) corresponding to the regions of minimum and maximum electron densities, respectively. Neutral GW wind perturbations (with zonal and vertical components anti-correlated) are shown with blue arrows, and the black circle shows the expected plasma motion leading to instability growth in the westward and upward phase of plasma motion (Hysell *et al*., 2004). The pink region shows where neutral GW motions oppose horizontal plasma motions (increasing the neutral-plasma velocity difference by up to ~20%, thus amplifying polarization electric fields) and enhance the vertical electron density gradient, all of which enhance the expected plasma instability growth rates anticipated by Kudeki *et al*. (2007) in this region of the flow. *Thus, we conclude that GW perturbations may have substantial influences on plasma instability growth in two ways: 1) they may significantly enhance plasma instability growth rates through perturbations of the neutral and plasma quantities upon which the growth rates depend and 2) they may induce "seed" perturbations at suitable spatial scales, allowing more rapid attainment of finite-amplitude perturbations extending to higher altitudes.* Finally, the westward intrinsic phase speed of the hypothesized GW of $(c - U_n) \sim N\lambda_z/2\pi \sim 160$ m s^{-1} implies westward propagation, a phase motion close to that of the westward plasma drift, and hence a much longer time for coherent perturbations to act on the underlying plasma than suggested by the much higher GW intrinsic frequency. Similar arguments can be made about the potential effects of GWs propagating eastward or superpositions of GWs having various propagation directions (see Fritts *et al*., 2008b). These influences will vary with the relative contributions of the GW to horizontal and vertical velocity and plasma density gradient fluctuations. In either case, it appears to us that it is likely that large-amplitude GWs at the bottomside *F* layer contribute to growth of the plasma instabilities and plasma bubbles extending to much higher altitudes.

6. Summary of Initial SpreadFEx Results

While our summary of SpreadFEx analyses presented here is not complete, there are a number of preliminary statements that we can make about the neutral and plasma dynamics observed during the campaigns based on these results. We list here those results that appear to be defensible

at this stage, and refer readers to our forthcoming SpreadFEx special issue of *Annales Geophysicae* for more comprehensive analyses. Current conclusions include:

a) deep convection appears to be a significant and viable source of GWs penetrating into the MLT and to the bottomside *F* layer, depending on GW scales, frequencies, and propagation directions;
b) GWs spanning a wide range of scales and frequencies can reach the MLT, but only GWs having large scales and high frequencies can reach higher altitudes;
c) GWs arising from convection are strongly influenced by lower atmospheric and MLT winds that dictate which GW frequencies, scales, and propagation directions allow penetration to the bottomside *F* layer and above;
d) digisonde electron densities suggest GWs having downward phase motions (upward propagation), periods of ∼20 min to 2 hr, and significant electron density perturbations at the bottomside *F* layer, with corresponding implied neutral density and wind perturbations;
e) GPS data suggest GWs of similar periods extending to even higher altitudes before and after plasma bubble occurrence;
f) smaller-scale GWs and wave-mean flow interactions appear to excite bores in the MLT that exhibit a variety of dispersive and nonlinear responses;
g) VHF radar and digisonde data suggest a connection between rising plasma motions, decreasing electron densities, increasing plasma gradients, and plasma bubble initiation;
h) VHF radar, digisonde, GPS, airglow, and GUVI data suggest an ability to quantify plasma perturbations in altitude, longitude, and time; however, it remains unclear how these perturbations are related to plasma bubble generation;
i) neutral zonal tidal winds appear to play an important role in enabling spread *F* seeding, given the transition from westward to eastward neutral motions at ∼250 km and above in the early evening hours;
j) the multiple correlative data sets collected during the SpreadFEx campaigns are among the most comprehensive available, and will likely enable more quantitative conclusions upon completion of our various analyses;
k) our initial results lead us to conclude that GWs may have sufficient perturbation amplitudes and impacts on instability growth rate at the bottomside *F* layer that their potential role in ESF and plasma bubble seeding should not be discounted;

and

l) it remains to be quantified fully how the GW neutral and electron density perturbations identified in our SpreadFEx experiment affect the generation of ESF and plasma bubbles extending to higher altitudes.

Acknowledgments. The SpreadFEx field program and data analysis were supported by NASA under contracts NNH04CC67C and NAS5-02036. Related modeling and theoretical activities were supported by NSF grants ATM-0314060 and ATM-0537311 and AFOSR contract FA9550–06-C-0129. We also thank M. R. Hausman and L. J. Nickisch for their assistance in analyzing GPS data from Fortaleza and V. T. Rampinelli, E. Bataglin, J. Sempere, N. D. Cândido, and the São João d'Aliança's House of Representatives and São João d'Aliança's Mayor's House for local support during the campaign. CPTEC-INPE provided assistance with the GOES 12 data analysis. Some of the authors also had partial support from Conselho Nacional de Desenvolvimento Cietifico e Tecnologico CNPq (Abdu, Sobral, de Paula, I. Batista, Takahashi, and Gobbi). Finally, we thank Wenbin Wang and two anonymous reviewers for helpful comments on the manuscript.

References

Abdu, M. A., Outstanding problems in the equatrial ionosphere-thermosphere system relevant to spread *F*, *J. Atmos. Sol.-Terr. Phys.*, **63**, 869, 2001.

Abdu, M. A., I. S. Batista, and J. H. A. Sobral, A new aspect of magnetic control of equatorial spread *F*, *J. Geophys. Res.*, **97**, 14,897, 1992.

Abdu, M. A., I. S. Batista, H. Takahashi, J. MacDougall, J. H. Sobral, A. F. Medeiros, and N. B. Trivedi, Magnetospheric disturbance induced equatorial plasma bubble development and dynamics: A case study in Brazilian sector, *J. Geophys. Res.*, **108**(A12), 1449, doi:10.1029/2002JA009721, 2003.

Abdu, M. A., E. A. Kherani, I. S. Batista, E. R. de Paula, and D. C. Fritts, An evaluation of the ESF/bubble irregularity growth conditions under gravity wave influences based on observational data from the SpreadFEx campaign, *Ann. Geophys.*, SpreadFEx special issue, 2008 (submitted).

Aggson, T. L., N. C. Maynard, W. B. Hanson, and L. Saba Jack, Electric field observations of equatorial bubbles, *J. Geophys. Res.*, **97**, 2997, 1992.

Anderson, D. N., A. D. Richmond, B. B. Balsley, R. G. Roble, M. A. Biondi, and D. P. Sipler, In situ generation of gravity waves as a possible seeding mechanism for equatorial spread-*F*, *Geophys. Res. Lett.*, **9**, 789–792, 1982.

Basu, B., On the linear theory of equatorial plasma instability: comparison of different descriptions, *J. Geophys. Res.*, **107**(A8), doi:10.1029/2001JA000317, 2002.

Batista, I. S. and M. A. Abdu, Ionospheric variability at Brazilian low and equatorial latitudes: comparison between observations and IRI model, *Adv. Space Res.*, **34**, 1894–1900, 2004.

Batista, P. P., B. R. Clemesha, A. S. Tokumoto, and L. M. Lima, Structure of the mean winds and tides in the meteor region over Cachoeira Paulista, Brazil (22.7°S,45°W) and its comparison with models, *J. Atmos. Sol.-Terr. Phys.*, **66**(6–9), 623–636, 2004.

Batista, I. S., M. A. Abdu, A. J. Carrasco, B. W. Reinisch, E. R. de Paula, and N. J. Schuch, Equatorial spread *F* and sporadic *E*-layer connections during the Brazilian Conjugate Point Equatorial Experiment—COPEX, *J. Atmos. Sol.-Terr. Phys.*, 2008 (in press).

Buriti, R. A., W. K. Hocking, P. P. Batista, A. F. Medeiros, and B. R. Clemesha, Observations of equatorial mesospheric winds over Cariri (7.4 S) by a meteor radar and comparison with existing models, *Ann. Geophys.*, 2007 (submitted).

Calais, E. and J. B. Minster, GPS, earthquakes, the ionosphere, and the Space Shuttle, *Phys. Earth Planet. Inter.*, **105**(3–4), 167–181, 1998.

Calais, E., J. S. Haase, and J. B. Minster, Detection of ionospheric perturbations using a dense GPS array in Southern California, *Geophys. Res. Lett.*, **30**(12), 2003.

de Paula, E. R. and D. L. Hysell, The São Luis 30 MHz coherent scatter ionospheric radar: system description and initial results, *Radio Sci.*, **39**, RS1014, doi:10.1029/2003RS002914, 2004.

Dewan, E. M. and R. H. Picard, Mesospheric bores, *J. Geophys. Res.*, **103**(D6), 6295–6306, 1998.

Dewan, E. M. and R. H. Picard, On the origin of mesospheric bores, *J. Geophys. Res.*, **106**(D3), 2921–2928, 10.1029/2000JD900697, 2001.

Djuth, F. T., M. P. Sulzer, J. H. Elder, and V. B. Wickwar, High-resolution studies of atmosphere-ionosphere coupling at Arecibo Observatory, Puerto Rico, *Radio Sci.*, **32**, 2321–2344, 1997.

Djuth, F. T., M. P. Sulzer, S. A. Gonzales, J. D. Mathews, J. H. Elder, and R. L. Walterscheid, A continuum of gravity waves in the Arecibo

thermosphere?, *Geophys. Res. Lett.*, **31**, doi:10.1029/2003GL019376, 2004.

Fechine, J., A. F. Medeiros, R. A. Buriti, H. Takahashi, and D. Gobbi, Mesospheric bore events in the equatorial middle atmosphere, *J. Atmos. Sol.-Terr. Phys.*, **67**, 1774–1778, 2005.

Fechine, J., C. M. Wrasse, H. Takahashi, A. F. Medeiros, P. P. Batista, B. R. Clemesha, L. M. Lima, D. Fritts, M. J. Taylor, P. D. Paulet, M. G. Mlynczak, and J. M. Russell, Mesospheric bore event during SpreadsFEx campaign, *Ann. Geophys.*, SpreadFEx special issue, 2008 (submitted).

Fejer, B. G., Natural ionospheric plasma waves, in *Modern Ionospheric Science*, edited by H. Kohl, R. Rüster, and K. Schlegel, pp. 217–273, Max-Planck Institut für Aeronomie, Lindau, Germany, 1996.

Fejer, B. G., L. Scherliess, and E. R. de Paula, Effects of the vertical plasma drift velocity on the generation and evolution of equatorial spread F, *J. Geophys. Res.*, **104**, 19,859, 1999.

Fritts, D. C. and L. Yuan, An analysis of gravity wave ducting in the atmosphere: Eckart's resonances in thermal and Doppler ducts, *J. Geophys. Res.*, **94**(D15), 18,455–18,466, 1989.

Fritts, D. C. and M. J. Alexander, Gravity dynamics and effects in the middle atmosphere, *Rev. Geophys.*, **41**, doi:10.1029/2001RG000106, 2003.

Fritts, D. C. and S. A. Vadas, Gravity wave penetration into the thermosphere: Sensitivity to solar cycle variations and mean winds, *Ann. Geophys.*, 2008 (in press).

Fritts, D. C. *et al.*, Overview and summary of the spread F Experiment (SpreadFEx), *Ann. Geophys.*, SpreadFEx special issue, 2008a (in press).

Fritts, D. C. *et al.*, Gravity wave and tidal influences on equatorial spread F based on observations during the spread F Experiment (SpreadFEx), *Ann. Geophys.*, SpreadFEx special issue, 2008b (submitted).

Haerendel, G., J. V. Eccles, and S. Cakir, Theory of modeling the equatorial evening ionosphere and the origin of the shear in the horizontal plasma flow, *J. Geophys. Res.*, **97**, 1209–1223, 1992.

Heelis, R. A., P. C. Kendall, R. J. Moffett, D. W. Windel, and H. Rishbeth, Electrical coupling of the E and F regions and its effect on F-region drifts and winds, *J. Planet. Space Sci.*, **22**, 743, 1974.

Hocke, K. and K. Schlegel, A review of atmospheric gravity waves and traveling ionospheric disturbances: 1982–1995, *Ann. Geophys.*, **14**, 917–940, 1996.

Hofmann-Wellenhof, B., *Global Positioning System: theory and practice*, 355 pp., Springer-Verlag, New York, 1994.

Huang, C. S. and M. C. Kelley, Nonlinear evolution of equatorial spread-F. 1. On the role of plasma instabilities and spatial resonance associated with gravity wave seeding, *J. Geophys. Res.*, **101**, 283, 1996a.

Huang, C. S. and M. C. Kelley, Nonlinear evolution of equatorial spread-F. 2. Gravity wave seeding of Rayleigh-Taylor instability, *J. Geophys. Res.*, **101**, 293, 1996b.

Huang, C. S. and M. C. Kelley, Nonlinear evolution of equatorial spread-F. 4. Gravity waves, velocity shear, and day-to-day variability, *J. Geophys. Res.*, **101**, 24,523, 1996c.

Huang, C. S., M. C. Kelley, and D. L. Hysell, Nonlinear Rayleigh-Taylor instabilities, atmospheric gravity waves, and equatorial spread-F, *J. Geophys. Res.*, **98**, 15,631, 1993.

Huang, C. S., J. C. Foster, L. P. Goncharenko, G. D. Reeves, J. L. Chau, K. Yumoto, and K. Kitamura, Variations of low-latitude geomagnetic fiels and Dst index caused by magnetospheric substorms, *J. Geophys. Res.*, **109**, A05219, doi:10.1029/2003JA010334, 2004.

Hysell, D. L., Radar imaging of equatorial F region irregularities with maximum entropy interferometry, *Radio Sci.*, **31**(6), 1567–1578, 1996.

Hysell, D. L. and J. D. Burcham, Long term studies of equatorial spread F using the JULIA radar at Jicamarca, *J. Atmos. Sol.-Terr. Phys.*, **64**, 1531–1543, 2002.

Hysell, D. L. and E. Kudeki, Collisional shear instability in the equatorial F region ionosphere, *J. Geophys. Res.*, **109**, A11301, doi:10.1029/2004JA010636, 2004.

Hysell, D. L., M. C. Kelley, W. E. Swartz, and R. F. Woodman, Seeding and layering of equatorial spread-F, *J. Geophys. Res.*, **95**, 17,253, 1990.

Hysell, D. L., J. Chun, and J. L. Chau, Bottom-type scattering layers and equatorial spread F, *Ann. Geophys.*, **22**, 4061, 2004.

Hysell, D. L., M. F. Larsen, C. M. Swenson, A. Barjatya, T. F. Wheeler, M. F. Sarango, R. F. Woodman, and J. L. Chau, Onset conditions for equatorial spread F determined during EQUIS II, *Geophys. Res. Lett.*, **32**, L24104, doi:10.1029/2005GL024743, 2005.

Kamalabadi, F. *et al.*, Electron densities in the lower thermosphere from GUVI 1356 tomographic inversions in support of SpreadFEx, *Ann. Geophys.*, SpreadFEx special issue, 2008 (submitted).

Kelley, M. C., *The Earth's Ionosphere*, 487 pp., Academic Press, San Diego, 1989.

Kelley, M. C. and D. L. Hysell, Equatorial spread F and neutral atmospheric turbulence: a review and a comparative anatomy, *J. Atmos. Terres. Phys.*, **53**, 695–708, 1991.

Kelley, M. C., M. F. Larsen, C. LaHoz, and J. P. McClure, Gravity wave initiation of equatorial spread F: A case study, *J. Geophys. Res.*, **86**, 9087–9100, 1981.

Keskinen, M. J., S. L. Ossakow, and P. K. Chaturvedi, Preliminary report of numerical simulations of intermediate wavelength collisional Rayleigh-Taylor instability in equatorial spread-F, *J. Geophys. Res.*, **85**, 1775, 1980.

Keskinen, M. J., S. L. Ossakow, S. Basu, and P. Sultan, Magnetic flux tube integrated evolution of equatorial ionospheric plasma bubbles, *J. Geophys. Res.*, **103**, 3957, 1998.

Keskinen, M. J., S. L. Ossakow, and B. G. Fejer, Three-dimensional nonlinear evolution of equatorial ionospheric spread-F bubbles, *Geophys. Res. Lett.*, **30**, 1855, doi:10.1029/2003GL017418, 2003.

Kherani, E. A., M. A. Abdu, E. R. de Paula, D. C. Fritts, J. H. A. Sobral, and F. C. de Meneses Jr., The impact of gravity waves rising from convection in the lower atmosphere on the generation and nonlinear evolution of equatorial plasma bubbles, *Ann. Geophys.*, SpreadFEx special issue, 2008 (submitted).

Klostermeyer, J., Nonlinear investigation of the spatial resonance effect in the nighttime equatorial F region, *J. Geophys. Res.*, **83**, 3753, 1978.

Kudeki, E., A. Akgiray, M. Milla, J. L. Chau, and D. L. Hysell, Equatorial spread-F initiation: post-sunset vortex, thermospheric winds, gravity waves, *J. Atmos. Sol.-Terr. Phys.*, **69**, 2416–2427, 2007.

Kudeki, E. and S. Bhattacharyya, Postsunset vortex in equatorial F-region plasma drifts and implications for bottomside spread F, *J. Geophys. Res.*, **104**, 28,163, 1999.

Lane, T. P. and R. D. Sharman, Gravity wave breaking, secondary wave generation, and mixing above deep convection in a three-dimensional cloud model, *Geophys. Res. Lett.*, **33**, L23813, doi:10.1029/2006GL027988, 2006.

Lane, T. P., M. J. Reeder, and T. L. Clark, Numerical modeling of gravity waves generated by deep tropical convection, *J. Atmos. Sci.*, **58**, 1249–1274, 2001.

Lane, T. P., R. D. Sharman, T. L. Clark, and H.-M. Hsu, An investigation of turbulence generation mechanisms above deep convection, *J. Atmos. Sci.*, **60**, 1297–1321, 2003.

Lanyi, G. E. and T. Roth, A comparison of mapped and measured total ionospheric electron-content using global positioning system and beacon satellite-observations, *Radio Sci.*, **23**(4), 483–492, 1988.

Laughman, B., D. C. Fritts, and J. Werne, Numerical simulation of bore generation and morphology in thermal and Doppler ducts, *Ann. Geophys.*, SpreadFEx special issue, 2008 (submitted).

McClure, J. P., W. B. Hanson, and J. F. Hoffman, Plasma bubble and irregularities in the equatorial ionosphere, *J. Geophys. Res.*, **82**, 2650, 1977.

McClure, J. P., S. Singh, D. K. Bamgboye, F. S. Johnson, and H. Kil, Occurrence of equatorial F region irregularities: Evidence for tropospheric seeding, *J. Geophys. Res.*, **103**, 29,119–29,135, 1998.

Medeiros, A. F., R. A. Buriti, E. A. Machado, H. Takahashi, P. P. Batista, D. Gobbi, and M. J. Taylor, Comparison of gravity wave activity observed by airglow imaging at two different latitudes in Brazil, *J. Atmos. Sol.-Terr. Phys.*, **60**, 647–654, 2004.

Medeiros, A. F., J. Fechine, R. A. Buriti, H. Takahashi, C. M. Wrasse, and D. Gobbi, Response of OH, O_2, and OI5577 airglow emissions to the mesospheric bore in the equatorial region of Brazil, *Adv. Space Res.*, **35**, 1971–1975, 2005.

Mendillo, M. and A. Tyler, The geometry of depleted plasma regions in the equatorial ionosphere, *J. Geophys. Res.*, **88**, 5778, 1983.

Meriwether, J., M. Faivre, C. Fesen, P. Sherwood, and O. Veliz, New results on equatirla thermospheric winds and the midnight temperature maximum, *Ann. Geophys.*, 2008 (in press).

Oliver, W. L., Y. Otsuka, M. Sato, T. Takami, and S. Fukao, A climatology of F region gravity wave propagation over the middle and upper atmosphere radar, *J. Geophys. Res.*, **102**, 14,499–14,512, 1997.

Ossakow, S. L., Spread-F theories—A review, *J. Atmos. Terres. Phys.*, **43**, 437, 1981.

Piani, C., D. Durran, M. J. Alexander, and J. R. Holton, A numerical study of three-dimensional gravity waves triggered by deep tropical convection, *J. Atmos. Sci.*, **57**, 3689–3702, 2000.

Prakash, S., Production of electric field perturbations by gravity wave winds in the E region suitable for initiating equatorial spread F, *J.*

Geophys. Res., **104**, 10,051–10,069, 1999.

Rodrigues, F. S., E. R. de Paula, M. A. Abdu, A. C. Jardim, K. N. Iyer, P. M. Kintner, and D. L. Hysell, Equatorial spread *F* irregularity characteristics over São Luis, Brazil, *Radio Sci.*, **39**, doi:10.1029/2002RS002826, 2004.

Scannapieco, A. J. and S. L. Ossakow, Nonlinear spread-*F*, *Geophys. Res. Lett.*, **3**, 451, 1976.

Sekar, R. and M. C. Kelley, On the combined effects of vertical shear and zonal electric field patterns on nonlinear equatorial spread *F* evolution, *J. Geophys. Res.*, **103**, 20,735–20,747, 1998.

Sekar, R., R. Suhasini, and R. Raghavarao, Evolution of plasma bubbles in the equatorial *F* region with different seeding conditions, *Geophys. Res. Lett.*, **22**, 885, 1995.

Sentman, D. D., E. M. Wescott, R. H. Picard, J. R. Winick, H. C. Stenbaek-Nielson, E. M. Dewan, D. R. Moudry, F. T. São Sabbas, and M. J. Heavner, Simultaneous observation of mesospheric gravity waves and sprites generated by a Midwestern thunderstorm, *J. Atmos. Sol.-Terr. Phys.*, **65**, 537–550, 2003.

Seyler, C. E., Internal waves and undular bores in mesospheric inversion layers, *J. Geophys. Res.*, **110**, D09S05, doi:10.1029/2004JD004685, 2005.

Sobral, J. H. A., M. A. Abdu, and I. S. Batista, Airglow studies on the ionosphere dynamics over low latitude in Brazil, *Ann. Geophys.*, **36**(2), 199–204, 1980a.

Sobral, J. H. A., M. A. Abdu, I. S. Batista, and C. J. Zamlutti, Association between plasma bubble and airglow disturbances over Brazilian low latitudes, *Geophys. Res. Lett.*, **11**(7), 980–982, 1980b.

Sobral, J. A. H., H. Takahashi, M. A. Abdu, M. J. Taylor, H. Sawant, D. C. Santana, D. Gobbi, A. F. de Medeiros, C. J. Zamlutti, N. J. Schuch, and G. L. Borba, Thermospheric *F*-region travelling disturbances detected at low latitude by an OI (630 nm) imager system, *Adv. Space Sci.*, **27**, 1201–1206, 2001.

Sobral, J. H. A, M. A. Abdu, H. Takahashi, M. J. Taylor, E. R. de Paula, C. J. Zamlutti, and G. L. Borba, A study of the ionospheric plasma bubbles climatology over Brazil, based on 22 years (1977–1998) of OI 630 nm airglow observation, *J. Atmos. Terr. Phys.*, **64**(12–14), 1517–1524, 2002.

Stolle, C., H. Luhr, M. Rother, and G. Balasis, Magnetic signatures of equatorial spread *F* as observed by the CHAMP satellite, *J. Geophys. Res.*, **111**, A02304, doi:10.1029/2005JA011184, 2006.

Su, S.-Y., C. K. Chao, and C. H. Liu, On monthly/seasonal/longitudinal variations of equatorial irregularity occurrencesand their relationship with the postsunset vertical drift velocities, *J. Geophys. Res.*, **113**, A05307, doi:10.1029/2007JA012809, 2008.

Sultan, P. J., Linear theory and modeling of the Rayleigh Taylor instability leading to the occurrence of equatorial spread *F*, *J. Geophys. Res.*, **101**, 26875–26891, 1996.

Swartz, W. E. and R. F. Woodman, Same night observations of spread-*F* by the Jicamarca Radio Observatory in Peru and CUPRI in Alcantara, Brazil, *Geophys. Res. Lett.*, **25**, 17–20, 1998.

Takahashi, H., M. J. Taylor, P.-D. Pautet, A. F. Medeiros, D. Gobbi, C. M. Wrasse, J. Fechine, M. A. Abdu, I. S. Batista, E. Paula, J. H. A. Sobral, D. Arruda, S. Vadas, F. S. Sabbas, and D. Fritts, Simultaneous observation of ionospheric plasma bubbles and mesospheric gravity waves during the SpreadFEx Campaign, *Ann. Geophys.*, SpreadFEx special issue, 2008 (in review).

Taylor, M. J. and M. A. Hapgood, Identification of a thunderstorm as a source of short period gravity waves in the upper atmospheric nightglow emissions, *Planet. Space Sci.*, **36**, 975, 1988.

Taylor, M. J., J.-M. Jahn, S. Fukao, and A. Saito, Possible evidence of gravity wave coupling into the mid-latitude *F* region ionosphere during the SEEK campaign, *Geophys. Res. Lett.*, **25**, 1801–1804, 1998.

Taylor, M. J. *et al.*, Gravity waves in the OH airglow layer observed during the SpreadFEx campaign in Brazil, SpreadFEx special issue, *Ann. Geophys.*, 2008 (submitted).

Taylor, M. J., P. D. Pautet, A. F. Medeiros, R. Buriti, J. Fechine, D. C. Fritts, S. Vadas, H. Takahashi, and F. São Sabbas, Characterizing mesospheric gravity waves near the magnetic equator, Brazil during the SpreadFEx campaign, *Ann. Geophys.*, SpreadFEx special issue, 2008 (submitted).

Tsuda, T., M. Nishida, and C. Rocken, A global morphology of gravity wave activity in the stratosphere revealed by the GPS occultation data (GPS/MET), *J. Geophys. Res.*, **105**, 7257–7274, 2000.

Tsunoda, R. T., Time evolution and dynamics of equatorial backscatter plumes: 1. Growth phase, *J. Geophys. Res.*, **86**, 139–149, 1981.

Tsunoda, R. T., On the enigma of day-to-day variability in equatorial spread *F*, *Geophys. Res. Lett.*, **32**, L08103, doi:10.1029/2005GL022512, 2005.

Tsunoda, R. T., Day-to-day variability in equatorial spread *F*: Is there some physics missing?, *Geophys. Res. Lett.*, **33**, L16106, doi:10.1029/2006GL025956, 2006.

Tsunoda, R. T., Seeding of equatorial plasma bubbles with electric fields from an E_s-layer instability, *J. Geophys. Res.*, **112**, A06304, doi:10.1029/2006JA012103, 2007.

Vadas, S. L., Horizontal and vertical propagation and dissipation of gravity waves in the thermosphere from lower atmospheric and thermospheric sources, *J. Geophys. Res.*, **112**, A06305, doi:10.1029/2006JA011845, 2007.

Vadas, S. L. and D. C. Fritts, Gravity wave radiation and mean responses to local body forces in the atmosphere, *J. Atmos. Sci.*, **58**, 2249–2279, 2001.

Vadas, S. L. and D. C. Fritts, The importance of spatial variability in the generation of secondary gravity waves from local body forces, *Geophys. Res. Lett.*, **29**(20), 10.1029/2002GL015574, 2002.

Vadas, S. L. and D. C. Fritts, Thermospheric responses to gravity waves arising from mesoscale convective complexes, *J. Atmos. Sol.-Terr. Phys.*, **66**, 781–804, 2004.

Vadas, S. L. and D. C. Fritts, Thermospheric responses to gravity waves: Influences of increasing viscosity and thermal diffusivity, *J. Geophys. Res.*, **110**, D15103, doi:10.1029/2004JD005574, 2005.

Vadas, S. L. and D. C. Fritts, The influence of increasing temperature and solar variability on gravity wave structure and dissipation in the thermosphere, *J. Geophys. Res.*, TIMED special issue, **111**, A10812, doi:10.1029/2005JA011510, 2006.

Vadas, S. L. and D. C. Fritts, Reconstruction of the gravity wave field from convective plumes via ray tracing, *Ann. Geophys.*, SpreadFEx special issue, 2008 (submitted).

Vadas, S. L., D. C. Fritts, and M. J. Alexander, Mechanism for the generation of secondary waves in wave breaking regions, *J. Atmos. Sci.*, **60**, 194–214, 2003.

Vadas, S. L., M. J. Taylor, P.-D. Pautet, P. Stamus, D. C. Fritts, F. São Sabbas, and V. Thiago, Convection: The likely source of the medium-scale gravity waves observed in the OH airglow layer near Brasilia, Brazil, during the SpreadFEx campaign, *Ann. Geophys.*, SpreadFEx special issue, 2008 (submitted).

Valladares, C. E., W. B. Hanson, J. P. McClure, and B. L. Cragin, Bottomside sinusoidal irregularities in the equatorial *F* region, *J. Geophys. Res.*, **88**, 8025, 1983.

Woodman, R. F. and C. LaHoz, Radio observations of *F*-region equatorial irregularities, *J. Geophys. Res.*, **85**, 5447, 1976.

Zalesak, S. T. and S. L. Ossakow, Nonlinear equatorial spread *F*: Spatially large bubbles resulting from large horizontal scale initial perturbations, *J. Geophys. Res.*, **85**, 2131, 1980.

Zalesak, S. T., S. L. Ossakow, and P. K. Chaturvedi, Nonlinear equatorial spread *F*: The effect of neutral winds and background Pedersen conductivity, *J. Geophys. Res.*, **87**, 151, 1982.

D. C. Fritts (e-mail: dave@cora.nwra.com), M. A. Abdu, B. R. Batista, I. S. Batista, P. P. Batista, R. Buriti, B. R. Clemesha, T. Dautermann, E. de Paula, B. J. Fechine, B. Fejer, D. Gobbi, J. Haase, F. Kamalabadi, B. Laughman, L. M. Lima, H.-L. Liu, A. Medeiros, P.-D. Pautet, D. M. Riggin, F. São Sabbas, J. H. A. Sobral, P. Stamus, H. Takahashi, M. J. Taylor, S. L. Vadas, and C. M. Wrasse